Author Manuscript

Author Manuscript

Author Manuscript

Author Manuscript

HHS Public Access

Author manuscript

Cell Rep. Author manuscript; available in PMC 2022 December 12.

Published in final edited form as:

Cell Rep. 2020 December 01; 33(9): 108446. doi:10.1016/j.celrep.2020.108446.

Nutrient Signaling, Stress Response, and Inter-organelle Communication Are Non-canonical Determinants of Cell Fate

N. Ezgi Wood[1,*], **Piya Kositangool**[1,2], **Hanaa Hariri**[1], **Ashley J. Marchand**[1,3], **W. Mike Henne**[1,4,*]

[1]Department of Cell Biology, UT Southwestern Medical Center, 6000 Harry Hines Blvd., Dallas, TX 75390, USA

[2]Paul L. Foster School of Medicine, Texas Tech University Health Sciences Center, 5001 El Paso Dr., El Paso, TX 79905, USA

[3]Department of Veterinary Pathobiology, Texas A&M University, College Station, TX 77843, USA

[4]Lead Contact

SUMMARY

Isogenic cells manifest distinct cellular fates for a single stress; however, the nongenetic mechanisms driving such fates remain poorly understood. Here, we implement a robust multi-channel live-cell imaging approach to uncover noncanonical factors governing cell fate. We show that in response to acute glucose removal (AGR), budding yeast undergoes distinct fates, becoming either quiescent or senescent. Senescent cells fail to resume mitotic cycles following glucose replenishment but remain responsive to nutrient stimuli. Whereas quiescent cells manifest starvation-induced adaptation, senescent cells display perturbed endomembrane trafficking and defective nucleus-vacuole junction (NVJ) expansion. Surprisingly, senescence occurs even in the absence of lipid droplets. Importantly, we identify the nutrient-sensing kinase Rim15 as a key biomarker predicting cell fates before AGR stress. We propose that isogenic yeast challenged with acute nutrient shortage contains determinants influencing post-stress fate and demonstrate that specific nutrient signaling, stress response, trafficking, and inter-organelle biomarkers are early indicators for long-term fate outcomes.

Graphical Abstract

This is an open access article under the CC BY-NC-ND license (http://creativecommons.org/licenses/by-nc-nd/4.0/).

*Correspondence: nezgiwood@gmail.com (N.E.W.), mike.henne@utsouthwestern.edu (W.M.H.).

AUTHOR CONTRIBUTIONS

Conceptualization, Methodology, Investigation, Data Curation, Software, Formal Analysis, Validation, Writing, and Visualization, N.E.W.; Strain Construction, Preliminary Data, and Formal Analysis, P.K.; TLC Experiments, Feedback on Data Interpretation and Writing, H.H.; Strain Construction, A.M.; Conceptualization, Methodology, Writing, Supervision, Funding Acquisition, W.M.H.

SUPPLEMENTAL INFORMATION

Supplemental Information can be found online at https://doi.org/10.1016/j.celrep.2020.108446.

DECLARATION OF INTERESTS

The authors declare no competing interests.

Author Manuscript Author Manuscript Author Manuscript Author Manuscript

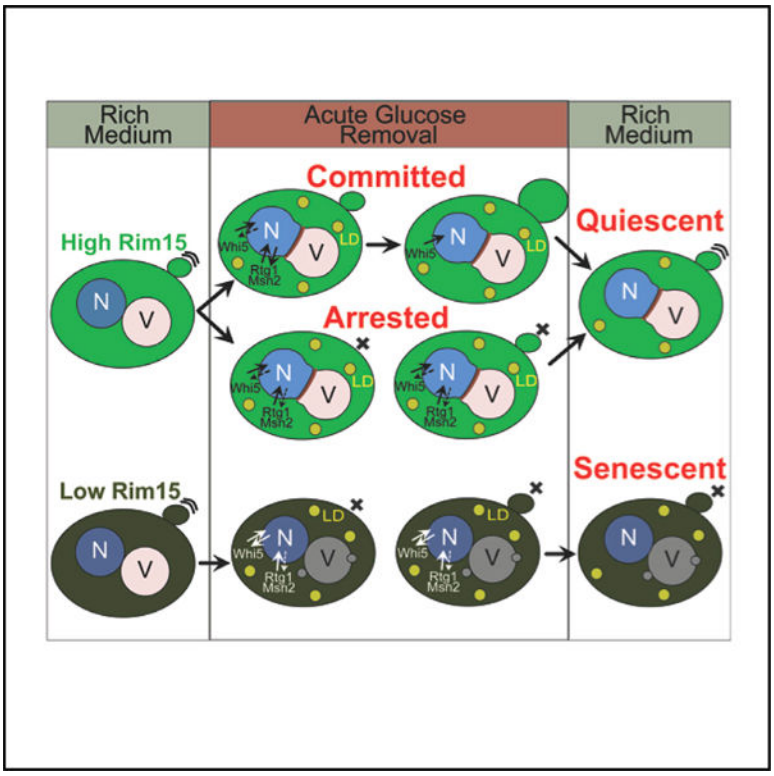

In Brief

Wood et al. show that nutrient signaling, inter-organelle crosstalk, stress response, and organelle homeostasis are early predictors of cell fate in quiescence/senescence decision in budding yeast. Using statistical evidence, they show that cells decide on their fate within 3–4 h upon nutrient stress before the cell fate manifests.

INTRODUCTION

To persist in an unpredictable environment, budding yeast must adapt to transitions between nutrient-rich and nutrient-poor conditions to maintain viability and proliferative capacity. Such adaptations are achieved through coordinated remodeling of numerous cellular systems encompassing nutrient sensing, stress response, inter-organelle communication, and metabolic and energy homeostasis pathways. Depending on the degree and type of nutrient deficiency, yeast starvation responses can result in diverse cell fates including quiescence, senescence, pseudohyphal growth, and meiosis (Honigberg, 2016). Importantly, different fates can co-exist in a population of genetically identical cells, implying non-genetic factors also govern cell fate decision-making (Aragon et al., 2008; Argüello-Miranda et al., 2018; De Virgilio, 2012; Laporte et al., 2018). Although starvation responses in yeast cultures have been extensively studied using bulk population-based methods, a key knowledge gap is understanding how the response to nutrient fluctuations is coordinated at the single-cell level and how this response diverges among cells with different fates within a clonal population.

Author Manuscript Author Manuscript Author Manuscript Author Manuscript

Glucose is a key carbon source for budding yeasts, and its acute removal induces dramatic changes in growth and metabolism (Broach, 2012). Glucose-starved cells suppress growth through inhibition of conserved TOR and PKA pathways (De Virgilio, 2012), halt mitotic cycles, and enter a non-proliferative state marked with significant transcriptional and metabolic remodeling as well as activation of stress responses (Görner et al., 2002). Glucose deprivation also drives organelle remodeling and promotes inter-organelle communication, as evidenced by the expansion of the nucleus-vacuole junction (NVJ), an inter-organelle contact site between the nuclear surface and yeast vacuole that physically grows following glucose removal (Hariri et al., 2018; Kvam and Goldfarb, 2006). Remarkably, upon re-exposure to glucose-rich medium, genetically identical yeast cells manifest distinct responses: some cells proliferate and resume budding (defined as quiescent cells), while others do not resume budding despite being metabolically active (defined as senescent cells) (Aragon et al., 2008; De Virgilio, 2012; Laporte et al., 2018; Werner-Washburne et al., 2011). How this cell fate is controlled in an isogenic population at the single-cell level is unresolved. Furthermore, how metabolic pathways and organelles communicate to drive these distinct fates remains poorly described. This is particularly true for senescent cells, which display increased lipid storage and lipid droplet (LD) biogenesis, although it is unclear what causative role LDs have in senescence itself (Flor et al., 2017).

Dissecting cell fate within isogenic populations has several technical challenges. First, widely adopted population-based methods often fail, since senescent and quiescent cells exist together. Second, there is no biomarker that unequivocally separates quiescent and senescent cells, apart from their ability to proliferate upon nutrient replenishment (Sagot and Laporte, 2019). This after-the-fact identification necessitates following single cells through the time course of starvation and nutrient replenishment. Additionally, since multiple pathways take part in adaptive metabolic remodeling, simultaneous measurements of several pathways are required at the single-cell level to dissect how these contribute to distinct cell fates.

Here, we overcome these challenges using a time-lapse imaging platform coupled to a microfluidics device and a computational analysis pipeline (Argüello-Miranda et al., 2018; Doncic et al., 2013; Wood and Doncic, 2019) that allows us to track single cells before, during, and after acute glucose removal (AGR), while simultaneously following five endogenously tagged fluorescent biomarkers. Using this system, we simultaneously tracked nutrient signaling, cell cycle, stress, metabolic, and inter-organelle contact site markers, and we dissect their relationships to cell fate.

RESULTS

Isogenic Cells Respond Differentially to AGR Stress

To interrogate the response of individual cells to acute glucose fluctuations, we developed an assay that merges time-lapse microscopy with microfluidics and allows us to follow individual cells before, during, and after AGR (Video S1). Specifically, yeasts in the exponential growth phase were loaded into the microfluidics device and grown for 2 h in rich media (SCD) and then exposed to AGR (SC) for 10 h. As expected, upon AGR exposure, all cells halted cell growth and budding. Next, cells were re-introduced to the

Author Manuscript Author Manuscript Author Manuscript Author Manuscript

glucose-rich medium for 4 h. Remarkably, upon this glucose replenishment, some cells resumed mitotic cycles and budding, while others did not (Figure 1A). Following the nomenclature in Laporte et al. (2018), we denote the growth-resuming cell population as quiescent and the non-resuming population as senescent. Note that here, quiescence and senescence are operationally defined, and other unknown conditions might lead to resumption of proliferation in the senescent cell population. Furthermore, time-lapse imaging throughout this process allowed us to distinguish two subpopulations of quiescent cells. As described below, one subpopulation completed one cell cycle during the AGR phase. We denote this subpopulation as quiescent-committed cells (Figure 1B). The other quiescent subpopulation arrested their cell cycle in AGR until glucose replenishment, regardless of their present stage of the cell cycle (Figure 1C). We define these as quiescent-arrested cells since they arrest their cell cycle during the AGR phase.

We tracked and segmented individual cells employing algorithms developed by Doncic et al. (2013) and Wood and Doncic (2019). Cell fates were scored semi-manually using both phase-contrast imaging and fluorescence imaging of the cell-cycle marker Whi5-mKoκ, which is an inhibitor of G1-S transition and resides in the nucleus during the G1 phase (Figures 1B–1D) (Di Talia et al., 2007). Specifically, we scored quiescence and senescence cell fates by monitoring bud emergence or bud growth after glucose replenishment using phase-contrast imaging. Quiescent-committed fate was scored using both bud growth and Whi5-mKoκ translocation into the nucleus of both mother and daughter during AGR. For budding yeast, the time of commitment to the mitotic cell cycle is denoted as ‘‘Start.’’ Once cells pass Start, they begin DNA replication, and the bud concomitantly emerges (Cross, 1995). Thus, we used yeast buds to determine the post-Start cells as in Jorgensen et al. (2002).

To understand the function and interplay of multiple pathways in this cellular decision process, we utilized our previously developed fluorescent protein tagging and imaging system, which allows for simultaneous monitoring of up to six fluorescent channels (Argüello-Miranda et al., 2018), to monitor protein biomarkers from a diverse array of cellular pathways (Videos S2 and S3). Here, we focused on biomarkers whose subcellular localizations and expression levels reported distinct aspects of cell and organelle metabolism and stress response, including a cell-cycle marker (Whi5); a stress-activated transcriptional activator linked to glucose deprivation (Msn2); a transcription factor that coordinates cross-talk between the nucleus and mitochondria to drive respiration (Rtg1); a marker for the NVJ inter-organelle contact site, which expands during glucose starvation (Nvj1); an energy and lipid storage marker that localizes to LDs (Erg6); a vacuole homeostasis marker (Vma1); and a stress-induced protein kinase linked to nutrient availability (Rim15) (Figures S1A–S1C). All lines contained Whi5-mKoκ, Erg6-mTFP1, Vma1-mNeptune2.5, and Nvj1-mRuby3 but differed in their markers for Msn2-mNeonGreen, Rtg1-mNeonGreen, or Rim15-mNeon-Green and are hence denoted WT-MSN2 (PK1359), WT-RTG1 (PK1701), and WT-RIM15 (PK1811 and AM45) (Figure 1E). When reporting joint markers, we pooled the data from WT-MSN2 and WT-RTG1 but presented their individual data in the Supplemental Information. Control experiments were conducted to confirm that these fluorescent markers did not grossly affect cell fitness and that they could be imaged together with minimal fluorescence bleed-through (STAR Methods; Table S1).

Author Manuscript Author Manuscript Author Manuscript Author Manuscript

AGR Induces Cell-Cycle Delay or Arrest at Any Stage of the Cell Cycle

First, we asked whether a distinct cell fate correlates with the cell-cycle stage the cell is in at the initiation of AGR. Because cells are not synchronized at the start of our assay, they were exposed to AGR at an arbitrary stage of their cell cycle. Following AGR initiation, all cells initially halted or postponed their cell cycle regardless of the cell-cycle stage they were in, suggesting that even cells in post-Start phase exhibit metabolic control on cell-cycle progression (Figures 1B–1D). As such, quiescent-committed cells initially halted cell-cycle progression but then completed one cell cycle during AGR and then arrested until glucose replenishment, as evidenced by Whi5-mKoκ nuclear translocation and bud growth during AGR (Figure 1B). Quiescent-committed cells represented 17.5% of cells (Table S2), and almost all quiescent-committed cells were post-Start (90.7%, 68/75; Table S3).

In contrast, quiescent-arrested cells halted their cell cycle during AGR until glucose replenishment, as evidenced by the lack of bud growth and emergence (Figure 1C). Quiescent-arrested cells constituted roughly half of all cells monitored (54.1%, 232/429; Table S2). Of these, a slim majority (64.7%) were pre-Start cells (Table S2). Thus, our data suggest that post-Start cells are more likely to complete their cell cycle during AGR and become quiescent committed ($p < 0.01$, Chi-square test). However, when we pool the quiescent-committed and quiescent-arrested cells together, we find that about half of all quiescent cells are pre-Start (51.1%; Table S3), whereas 63.1% of senescent cells are pre-Start (Figure 1D; Table S3). This indicates that the ability to resume mitotic cycles upon glucose replenishment does not depend on the cell-cycle stage at the time of AGR initiation ($p = 0.02$, Chi-square test).

Collectively, we find that AGR stress halts or delays the cell cycle of all cells regardless of their cell-cycle stage. Quiescent cells that were post-Start upon AGR initiation were more likely to complete their cell cycle during the AGR phase, but the ability to resume mitotic cycles following glucose replenishment is not related to the cell-cycle stage during AGR.

Cell Populations Display Temporally Unique Whi5 Translocation Profiles

To more thoroughly dissect the cell-cycle behavior of individual cells relative to one another, we plotted the nuclear Whi5-mKoκ signal of all monitored cells as a heatmap over the 16-h experimental time course (Figures 1F and S1F). Although there was some cell-to-cell variation, the nuclear retention of Whi5-mKoκ throughout AGR was distinct for each cell fate population (Figure 1F). For example, quiescent-committed cells completed their cell cycles at different times within the AGR experimental time, upon which Whi5-mKoκ simultaneously entered the nucleus of the mother and daughter cells (Figures 1B and 1F). Surprisingly, in a subpopulation of post-Start quiescent-committed cells, Whi5-mKoκ translocated into the nucleus of the mother during AGR but then translocated out of nucleus to the cytoplasm, then re-translocated into the nucleus of both the mother and the daughter later in the AGR phase (39.7%, 27/68; Figure S1D). Nearly all (85.4%, 70/82) post-Start quiescent-arrested cells also translocated Whi5-mKoκ into the nucleus during AGR (Figures 1D and 1F). Among a majority of quiescent cells (i.e., committed and arrested), nuclear Whi5-mKoκ was generally persistent, remaining until the end of AGR phase (Figure 1F). Collectively, these data suggest that quiescent cells accumulate Whi5-mKoκ in their nucleus

Author Manuscript Author Manuscript Author Manuscript Author Manuscript

during the AGR phase but surprisingly, even without completion of mitotic division, Whi5-mKoκ can translocate into the mother cell nucleus during AGR stress.

In contrast to quiescent cells, the majority of senescent cells accumulated the nuclear Whi5-mKoκ signal shortly after AGR initiation, but the Whi5-mKoκ nuclear signal gradually declined during the AGR phase (Figure 1F). In line with this, by the end of the AGR phase, 87.7% of senescent cells lost detectable Whi5-mKoκ nuclear signal. These observations indicate that cell fate populations respond differentially to sustained AGR stress and display unique temporal signatures of the cell-cycle inhibitor Whi5. They also suggest that Whi5-mKoκ accumulation and nucleus retention time during AGR may be a feature that distinguishes cell populations.

Quiescent and Senescent Cells Respond to AGR with Unique Stress Response Profiles

When examining senescent cells, we first verified that their cell fate was not due to fitness defects originating from their cell-cycle phase at AGR initiation, replicative age, doubling time, cell death, or delay in cell-cycle resumption (STAR Methods). To better characterize senescent cell behavior, we investigated whether senescent cells could sense nutrient stress and whether general stress pathways exhibit unique behaviors that correlated with specific cell fates. We generated chromosomally fluorescently tagged strains of Msn2 or Rtg1 expressed by their endogenous promoters. Msn2 is a stress-responsive transcriptional factor that translocates into the nucleus in response to a variety of stress conditions (Martínez-Pastor et al., 1996; Schmitt and McEntee, 1996). Rtg1 is a transcription factor that enters the nucleus following nutrient starvation and activates genes important to mitochondrial respiration (Butow and Avadhani, 2004; Chen et al., 2017; Liao and Butow, 1993). Remarkably, all cells translocated both Msn2 and Rtg1 into the nucleus within 6–18 min of AGR induction, indicating that cells of all fates sense and respond to AGR (Figures 2A and 2B). However, individual cells within each population displayed different temporal signatures of Msn2 or Rtg1 nuclear export during AGR. All quiescent-committed cells exported Msn2 and Rtg1 out of the nucleus before they completed their cell cycles (Figures 2A, 2B, S2A, and S2B), suggesting that cell-cycle progression may occur after the downregulation of Msn2- and Rtg1-associated nuclear signaling. In contrast, quiescent-arrested and senescent cells generally exhibited more sustained nuclear Msn2 and Rtg1 signals. In fact, 40.0% (52/130) of the quiescent-arrested cells and 45.8% (33/72) of the senescent cells exhibited extended Msn2 nuclear signal, as calculated by comparing the Msn2 nuclear levels between the sixth and seventh hours of AGR to basal Msn2 levels (Figure 2A; STAR Methods). By a similar calculation, 11.8% (12/102) of quiescent-arrested cells and 18% (9/50) of senescent cells exhibited sustained Rtg1 nuclear signal (Figure 2B; STAR Methods). Note that nuclear Msn2 and Rtg1 dynamics were not explained by the cell-cycle stage at the beginning of AGR (Figure S2C). Collectively, this indicates that different cell populations display temporally distinct stress response nuclear profiles during AGR, with quiescent-arrested and senescent cells generally exhibiting more sustained nuclear Msn2 and Rtg1 nuclear signals compared to quiescent-committed cells.

Author Manuscript Author Manuscript Author Manuscript Author Manuscript

Senescent Cells Execute Endocytosis in Response to Nutrient Cues but Exhibit Defects in Post-endocytic Endomembrane Trafficking

We next tested whether senescent cells are capable of responses to other stimuli. We monitored the endocytic uptake and trafficking of the methionine permease Mup1 as a stimuli-response test (Videos S4, S5, and S6). Mup1 is the primary methionine permease of budding yeast. When cells are grown in nutrient-rich media lacking methionine, Mup1 is primarily located on the plasma membrane (PM). Upon methionine addition or glucose starvation, Mup1 is endocytosed and trafficked into the vacuole for degradation (Lang et al., 2014). As such, Mup1 trafficking and subcellular localization enables us to monitor responsiveness to nutrient deprivation.

We generated diploid yeast (AM44) with one chromosomal copy of Mup1 tagged with the pH-sensitive fluorophore pHluorin, whose fluorescent signal is quenched when the cytoplasm is acidified upon glucose deprivation or when it is delivered into the acidic vacuole (Henne et al., 2012; Lin et al., 2008). The second Mup1 chromosomal copy was tagged with the pH-resistant fluorophore mKoκ. The vacuole was marked Vma1-mNeptune2.5 so that Mup1-mKoκ vacuole delivery could be monitored (Graham et al., 2003).

First, cells were grown in rich media lacking methionine (SCD-Met), where Mup1 accumulates at the PM. Cells were then exposed to AGR in media either containing or lacking methionine (SC+Met, SC-Met) for 10 h, followed by glucose replenishment in media containing methionine (SCD+Met), which should stimulate any residual Mup1 uptake (Lin et al., 2008). During AGR in either SC+Met or SC-Met, all quiescent-committed cells endocytosed Mup1-mKoκ and delivered it to the vacuole before they completed their cell cycles (Figures 2D–2F and S2D; Video S5). In contrast, 86.4% (408/472) of quiescent-arrested cells challenged with AGR in SC+Met media retained Mup1-mKoκ at the PM (Figures 2D and 2E). However, in AGR lacking both glucose and methionine (SC-Met), 71.8% (196/273) of quiescent-arrested cells endocytosed Mup1-mKoκ and trafficked it into the vacuole lumen (Figures 2F and S2D). This indicates that during AGR, most quiescent cells can endocytose Mup1-mKoκ, but quiescent-arrested cells preferentially retain Mup1-mKoκ at the PM if there is methionine in the culture medium.

In senescent cells during AGR in SC+Met media, Mup1-mKoκ remained at the PM and was not endocytosed (Figures 2D and 2E). However, upon glucose replenishment with SCD+Met, 67% (51/76) of the senescent cells endocytosed Mup1-mKoκ, whereas 32.9% (25/76) retained Mup1-mKoκ at the PM. This indicates that although senescent cells are non-proliferative, a majority are responsive to environmental cues and execute an endocytic response following sustained AGR (Figures 2C–2E). Indeed, 47.0% (39/83) of senescent cells internalized Mup1-mKoκ during AGR when cultured in SC-Met media, and 28.9% (24/83) of senescent cells endocytosed Mup1-mKoκ during the subsequent glucose replenishment (Figures 2F and S2D).

Next, we focused on Mup1-pHluorin to monitor cytoplasmic acidification (Dechant et al., 2010; Joyner et al., 2016). Immediately following AGR exposure, the cytoplasm of all cell populations acidified, as evidenced by Mup1-pHluorin signal loss (Figures 2E and

Author Manuscript Author Manuscript Author Manuscript Author Manuscript

2F). As expected, glucose replenishment returned the cytoplasm to a neutral pH, revealing Mup1-pHluorin localization. This showed that although a majority of senescent cells were able to successfully internalize Mup1 upon glucose replenishment, Mup1-pHluorin was not always successfully delivered into the vacuole lumen, where the pHluorin signal is quenched. In fact, in 49% (25/51) of senescent cells that endocytosed Mup1 after SC+Met AGR treatment, Mup1-pHluorin peri-vacuolar puncta accumulated within the yeast (Figure 2C, blue lined cells and white arrows). Consistent with this, Mup1-mKoκ also accumulated as bright punctae, indicating a defect in Mup1 vacuolar sorting (Figure 2C). In contrast, all quiescent cells eventually delivered and quenched Mup1-pHuorin in the vacuole (Figures 2C, green lined cells, and 2D–2F). This suggests that although senescent cells can execute Mup1 endocytosis following AGR, some aspect of post-endocytic endosomal trafficking and/or vacuole delivery is compromised.

In summary, in both quiescent and senescent cells, the cytoplasm acidifies during AGR, and they can execute endocytosis, indicating that they have the ability to remodel their PM in response to stress stimuli. Quiescent cells successfully deliver Mup1 into the vacuole. In contrast, only about half of senescent cells that endocytose Mup1 successfully delivered Mup1 into the vacuole, suggesting defects in endosome maturation or vacuole homeostasis that may underlie defects in senescent cell behavior.

Relative V-ATPase Assembly Differs among Quiescent and Senescent Cells

Since senescent cells displayed defects in post-endocytic endomembrane trafficking, we next investigated whether vacuole homeostasis was altered by monitoring the vacuolar ATPase (V-ATPase), which regulates intraluminal vacuole pH (Graham et al., 2003). The yeast V-ATPase is composed of two subcomplexes, whose reversible assembly controls V-ATPase function. Upon glucose removal, the V_1 subcomplex dissociates, whereas the V_0 subcomplex remains membrane associated. Because of its dissociation, the coefficient of variation (CoV) of V_1 subcomplex signal intensity has been shown to be a marker for relative V-ATPase assembly (Dechant et al., 2010). We monitored the CoV of Vma1-mNeptune2.5, a subunit of the V_1 subcomplex. As expected, the normalized Vma1-mNeptune2.5 CoV decreased for all cells during AGR. However, the signal decreased more drastically for senescent cells compared to quiescent cells (Figure S2E). Specifically, the CoV normalized to 1 at the beginning of AGR decreased to 0.65 ± 0.01 or quiescent cells but decreased to 0.59 ± 0.02 for senescent cells (mean ± SEM). Upon glucose replenishment, Vma1-mNeptune2.5 CoV increased for both quiescent and senescent cells but did not recover in senescent cells to the degree observed in quiescent cells (Figure S2E). As a control, we also monitored the normalized CoV of the Vph1-GFP, a subunit of the membrane-bound V_0 subcomplex. As expected, Vph1-GFP CoV did not significantly change during AGR (Figure S2F; 0.991 ± 0.033 for quiescent and 0.944 ± 0.023 for senescent; mean ± SEM). Collectively, the more drastic Vma1-mNeptune2.5 CoV change in senescent cells is consistent with altered vacuole homeostasis in this cell population.

Quiescent Cells Enlarge Their NVJ Contacts during AGR, but Senescent Cells Do Not

The vacuole does not function in isolation and is connected to other organelles, including the nucleus, that enable it to respond to stress. Since senescent cells exhibited altered

Author Manuscript Author Manuscript Author Manuscript Author Manuscript

endomembrane trafficking and vacuole homeostasis, we investigated whether the NVJ, a disc-shaped inter-organelle contact site that expands during nutrient deprivation, was also altered (Hariri et al., 2018; Henne and Hariri, 2018; Pan et al., 2000). We monitored chromosomally tagged Nvj1-mRuby3 to evaluate NVJ expansion during AGR (Figures 3A, S3A, and S3B). Remarkably, 87.7% of quiescent cells significantly increased Nvj1-mRuby3 signal during AGR, indicating NVJ expansion. In contrast, 80.3% of senescent cells did not increase Nvj1-mRuby3 signal during AGR (Figure 3B; STAR Methods). This suggests that failure to upregulate Nvj1 and expand the NVJ during AGR correlates with senescent cell fate.

Next, we queried whether Nvj1 loss would alter cell fates following AGR. We monitored WT and *nvj1*Δ yeast exposed to AGR, followed by glucose replenishment. Remarkably, *nvj1*Δ yeast displayed similar proportions of senescent and quiescent cells compared to the wild type (WT) (Table S2; Chi-square test, $p > 0.1$). We conclude that NVJ expansion is a correlative indictor of senescent cell fate after AGR but is not required for cell fate in our hands. We also cannot exclude that other endoplasmic reticulum (ER)-vacuole tethers such as Mdm1 or Ltc1/Lam6 may compensate for Nvj1 loss (Henne et al., 2015; Murley et al., 2015).

Cells Exhibit Enhanced Lipid Storage during AGR, but LDs Are Not Required for Cell Fates

The NVJ expands during starvation and serves as a platform for the local production of LDs, which store lipids during nutrient deprivation to promote cell survival (Hariri et al., 2018; Radulovic et al., 2013). Once glucose is resupplied, LDs can be mobilized to support new membrane synthesis and growth (Kohlwein et al., 2013). Since senescent cells generally failed to increase Nvj1-mRuby3 signal, we next investigated whether they also exhibited defects in lipid metabolism and LD biogenesis. We monitored LD biogenesis by imaging Erg6-mTFP1, an established LD marker and enzyme in the ergosterol biosynthetic pathway (Jacquier et al., 2011; Kristan and Rižner, 2012; Seo et al., 2017). Following AGR, Erg6-mTFP1 signal increased in every cell subpopulation, consistent with elevated LD biogenesis upon glucose removal (Figures 4A, 4B, and S4A–S4D). The fold increase in senescent cells was significantly lower than in quiescent cells (Figure 4C). Consistent with this increase in Erg6-mTFP1 signal, yeast cultures exhibited a slight elevation in triglycerides (TGs) and a significant elevation in ergosterol-esters (SE) during AGR exposure, as determined by thin layer chromatography (TLC) (Figure 4D). Glucose replenishment induced a further increase in TGs, but SE levels returned to pre-AGR levels, consistent with LD mobilization of SEs to provide sterols for new membrane synthesis (Figure 4D). In line with this, Erg6-mTFP1 signal decreased, on average, by 30.1% in quiescent cells. In contrast, Erg6-mTFP1 signal only decreased by 8% in senescent cells. This Erg6-mTFP1 signal decrease may be due to LD mobilization and/or due to protein dilution in cells that resumed budding.

LDs often accumulate in senescent cells, and cell senescence correlates with increased lipid synthesis (Flor et al., 2017; Lizardo et al., 2017). However, whether LDs are operationally required for senescence is unclear. Given that LDs are lipid reservoirs that contribute to yeast survival during long-term starvation (Seo et al., 2017; Wang, 2015), we next examined whether LDs are required for any cell fates following AGR. We compared the fates of WT

Author Manuscript Author Manuscript Author Manuscript Author Manuscript

cells with LD-deficient cells that lacked the enzymes required to produce TG (Dga1 and Lro1) and SE (Are1 and Are2) (ΔLD strain). Remarkably, this genetic perturbation caused a slight decrease in the number of senescent cells, but senescent cells were still detected within ΔLD yeast (Table S2; Figures 4E and S4E). We also examined whether yeast lacking the three major TG lipases also displayed altered cell fate proportions (*tgl3,4,5*ΔΔΔ strain). The *tgl3,4,5*ΔΔΔ yeast closely mimicked the ΔLD yeast with slightly reduced senescent cell numbers (Table S2; Figure 4E). Collectively, this suggests that cells of all fates increase LD storage during AGR stress. However, surprisingly, LDs are not required for quiescent or senescent cell fates in our experimental framework.

Pre-AGR Rim15 Levels Are Predictive of Post-AGR Cell Fate

Thus far, we find that quiescent and senescent cells exhibit differences in stress-response transcription factors, endomembrane trafficking dynamics, and NVJ expansion during or after AGR. However, prior to AGR, both senescent and quiescent cells exhibit similar levels of the protein biomarkers for these pathways, indicating that biomarker abundances provide no predictive power to designate cell fate prior to AGR (Figures 2A, 2B, 3B, and 4B). Given the possibility that cell fates might be emanating from some pre-existing heterogeneity within cells, we queried whether we could identify a biomarker whose fluorescent signal *before* AGR correlated to distinct cellular behaviors *after* AGR.

We hypothesized that proteins involved in nutrient signaling, particularly those naturally expressed at low levels, are strong candidates that may indicate cell fate prior to nutrient stress exposure. This is because low-abundance proteins display intrinsic cell-to-cell abundance variability, providing a mechanism for isogenic diversity. Using a candidate-based approach, we selected Rim15 as a potential predictor for several reasons. First, Rim15 is an effector kinase that is downstream of at least four major nutrient signaling pathways and regulates cell proliferation (Smets et al., 2010). Second, Rim15 is normally expressed at low levels in cycling cells (Lawless et al., 2016; Newman et al., 2006). We endogenously tagged Rim15 (Rim15-mNeonGreen, mNG) and monitored its mean intracellular intensity (Figures 5A and S5; Video S7).

Strikingly, elevated Rim15 levels prior to AGR were highly correlated with quiescence, whereas cells with low Rim15 before AGR were more likely to be senescent (Figures 5B and S5A). Specifically, 95.9% (47/49) of the cells with the highest Rim15-mNeonGreen levels were quiescent (denoted as cells that have higher Rim15-mNG levels than one SD from the mean at the initiation of AGR). In contrast, 88.9% (48/54) of senescent cells had lower-than-average Rim15-mNG intensity at the start of AGR. This percentage is 59.8% (177/296) for quiescent cells. This indicates that Rim15 levels before AGR correlate with cell fate after AGR.

Cells ‘‘Decide’’ Their Fates Prior to Glucose Replenishment

Next, using the biomarkers studied so far, we queried whether we could predict individual cell fates before glucose replenishment and, if so, how long before glucose replenishment. In Argüello-Miranda et al. (2018), we developed a theoretical framework using statistical evidence (Jaynes, 2003) to convert single-cell measurements into cell fate probabilities to

Author Manuscript Author Manuscript Author Manuscript Author Manuscript

predict individual cell fates before they manifested. Briefly, this is approached as a binary hypothesis testing problem, where we compare for a given cell the probabilities to become senescent or quiescent. To convert single-cell measurements into probabilities of cell fate, we first pool our measurements from cells of a given fate at a given time to estimate population distributions. Next, using these distributions, we calculate the likelihood of a given cell to belong to either of the two populations (STAR Methods).

To illustrate this method, we first used Nvj1-mRuby3 mean intensity, the most powerful single-parameter predictor for our cell fates (Figure 6A). Note that the Nvj1-mRuby3 signal distributions for quiescent and senescent cells were indistinguishable at the start of AGR; however, they gradually diverged throughout the AGR phase (quiescent [brown] and senescent [blue] distributions; Figure 6A). In fact, this was the case for all the biomarkers interrogated, except Rim15 (see below). Using Nvj1-mRuby3 distributions, we then predicted the cell fate of each cell and reported the percentage of correctly predicted cells using this approach (Figure 6A, back axis, dark blue). At the beginning of AGR, using Nvj1-mRuby3 data, around 50% of the cells are accurately assigned to their correct fate, essentially what a random guess would achieve (dark blue line, Figure 6A). However, as the population distributions of Nvj1-mRuby3 diverge, the percentage of correct predictions increases later in AGR. In fact, we accurately predict the fates of 81.9% of cells by the end of AGR.

Next, we combined the population distribution information from multiple biomarkers. Using this multi-parameter approach, by the completion of AGR, we correctly predict fates of 88.3% of WT cells (Figure 6B). Specifically, this percentage is 88.6% for WT-MSN2 and 88.1% for WT-RTG1 strains (Figure S6A). For WT-MSN2, we combined information from Nvj1, Msn2, Whi5, and Vma1 biomarkers; for WT-RTG1, we combined Nvj1, Rtg1, Whi5, and Vma1 (Figure S6A). Note that since Erg6-mTFP1 signal was increasing in both populations during AGR, it was not a strong predictor of cell fate. For a detailed discussion of parameters and parameter selection methodology, see the STAR Methods. Notably, cell size was also not a good predictor for quiescence/senescence decision (Figure S6B), although it is a strong predictor of meiosis, with over 90% accuracy (Argüello-Miranda et al., 2018; Day et al., 2004). This result is consistent with Laporte et al. (2018), showing that cell volume does not affect a cell's propensity for quiescence.

The fact that we accurately predicted fates of 82.1%–89.0% of the cells in the last 4 h of AGR (Figure 6B) indicates that quiescent and senescent populations exhibit already-diverged cellular biomarkers before glucose replenishment. Collectively, our data suggest that within our experimental system, yeast cells ''decide'' a fate (i.e., become predisposed to a specific fate) before that fate's manifestation (to cycle or not).

Rim15 Abundance Contains Information about Cell Fates before AGR

Next, we asked *when* individual cells ''decide'' on their fate, and thus we switched our focus from the percentage of correctly predicted cells to dissecting an individual cell's fate probabilities over time. Specifically, we examined the evolution of quiescence cell fate probabilities throughout AGR using cells whose fates were correctly predicted at the end of AGR via the combination of markers used in Figure 6B (Figures 6C and S6C;

Author Manuscript Author Manuscript Author Manuscript Author Manuscript

average probability of quiescence for quiescent [brown] and senescent [blue] cells). Note that the probability of quiescence was around 0.5 for both quiescent and senescent cells at the beginning of AGR (0.53 ± 0.01/0.55 ± 0.02 for quiescent/senescent; mean ± SEM). However, this probability steadily increased for quiescent cells during AGR and decreased for senescent cells, becoming 0.98 ± 0.004/0.03 ± 0.008 for quiescent/senescent cells at the end of AGR (mean ± SEM).

One exception to this was Rim15-mNG. Whereas both single parameters and the combination of parameters gave the probability of quiescence near 0.5 at the beginning of AGR (Figures 6C, S6C, and S6D), the probability of quiescence calculated using Rim15-mNG is 0.63 ± 0.01 for quiescent cells (n = 206) and 0.41 ± 0.01 (n = 47) for senescent cells (mean ± SEM) at the start of the AGR phase (Figure 6D). In fact, even 1 h before AGR initiation, these probabilities were 0.61 ± 0.01 and 0.41 ± 0.01, respectively, for quiescent and senescent cells. Thus, Rim15-mNG is the only biomarker that appeared to encode information about cell fate even *prior* to AGR. Although by itself Rim15-mNG was not a strong predictor for all cells (compare Figure S6E to Figures 6B and S6A), when we restricted our predictions to cells with signal one SD above or below the average Rim15-mNG signal, we accurately predicted their fate at 88.1% ± 3.4% (mean ± SD) throughout the entire AGR phase (Figure S6F). Applying the same procedure for predictions with Nvj1-mRuby3 area and mean intensity did not improve their overall predictive power (Figure S6F).

The Cell Fate Decision Occurs Early in the AGR Phase

When we analyzed the cell fate probabilities of individual cells calculated using the parameter combinations, we found that cells have a period where the probability of quiescence fluctuates around 0.5. However, there was a distinct point after which cell fate probabilities consistently pointed to one fate over another (Figure 6D). We have observed a similar point for the decision to undergo meiosis or not in our previous work (Argüello-Miranda et al., 2018), which we defined as the decision point (DP). We define the DP as the time point after which all predictions were correct for a given cell or, equivalently, after which the correct cell fate probability was always above 0.5.

Notably, the average DP is 3.6 h after AGR initiation (Figure 6E). Note that the average probability of quiescence is about 0.5 before DP for both quiescent and senescent cells (0.52 ± 0.1/0.52 ± 0.1 quiescent/senescent; mean ± SEM). After the DP, the probability for quiescent cells became almost 1 for quiescent cells and close to 0 for senescent cells (0.93 ± 0.05/0.10 ± 0.05 quiescent/senescent; mean ± SEM). Also, like the percentage of correctly predicted cells, the DP depends on the biomarkers used to calculate the cell fate probabilities. Thus, based on the biomarkers examined here, the majority of cells decide on a fate within 3–4 h of the initiation of a 10-h AGR phase, well before the manifestation of those cell fates.

It is important to note that the DP does not mark the *commitment point* to a cell fate, which is defined as the point of irreversibility, after which the cell will proceed with the fate even if the triggering signal (in this case, AGR exposure) is removed. To explain this further, when we varied our experimental protocol and exposed cells to AGR for only 3

Author Manuscript Author Manuscript Author Manuscript Author Manuscript

h, 99.1% (108/109) were quiescent, and 0.9% (1/109) were senescent. Similarly, when the cells were AGR treated for 5 h, 94.7% (107/113) were quiescent, and 5.3% (6/113) were senescent (Table S2). In Argüello-Miranda et al. (2018), we showed that the DP precedes the commitment point (i.e., the cell fate probabilities settled on a fate well before the cells underwent the first meiotic division), which marks the actual commitment to meiosis (Friedlander et al., 2006). Unlike meiosis, the commitment point to quiescence/senescence is not well defined and is beyond our scope here. Future studies will likely dissect how the DP and commitment point inter-relate during the important quiescence/senescence fate choice.

DISCUSSION

In the field of cellular decision-making, much focus is devoted to cell-fate-specific signaling (Balázsi et al., 2011), such as the cell-cycle machinery (Doncic et al., 2011). How general cellular homeostasis and organelle physiology affect fate decisions remains underexplored yet is critical to understanding adaptive metabolism. Here, we report that in response to AGR, isogenic yeasts manifest distinct quiescent and senescent fates correlating with temporally unique profiles (Figure 7). These are revealed by biomarkers associated with stress response, inter-organelle communication, and cellular metabolism. These biomarkers display diverging signal profiles throughout AGR. We also identify an early predictor, Rim15, whose cellular abundance prior to AGR is highly correlated to post-AGR cell fate.

Here, we employed a powerful framework to dissect the quiescence/senescence decision of yeast, allowing us to track single cells before, during, and after AGR while monitoring multiple biomarkers. In Argüello-Miranda et al. (2018), we combined our single-cell pipeline with a theoretical framework for forecasting cell fates and accurately predicted cell fates before the activation of cell-fate-specific signaling in meiosis. Here, we focus on the quiescence/senescence decision and show that this decision is made before return to glucose-rich media. Importantly, here and in Argüello-Miranda et al. (2018), we propose that cells manifest a DP, which marks the establishment of the predisposition for a cell fate but does *not* mark an irreversible commitment.

Our work also adds temporal understanding for the cell-cycle marker Whi5 and its relationship to glucose loss. We show that cells that pass Start will halt or postpone cell-cycle progression upon AGR. Whi5 also accumulates more in the nucleus in AGR compared to nutrient-rich media. Also, in a majority of post-Start cells that translocated Whi5 out of their nuclei before AGR, Whi5 translocates back into the nucleus during sustained AGR, indicating a return-to-G1 behavior. This suggests that Whi5 translocation out of the nucleus does not simply mark the commitment to the cell cycle in response to AGR. This surprising Whi5 behavior has been independently observed by at least two other labs (J.C. Ewald, personal communication; Qu et al., 2019).

Glucose starvation drives inter-organelle crosstalk and NVJ expansion. Surprisingly, we show that NVJ tether Nvj1 is a highly predictive marker for cell fate. Nearly all quiescent cells expand their NVJs during AGR, but senescent cells do not. Given that NVJs play important roles in lipid metabolism and autophagy (Roberts et al., 2003), this may indicate that NVJ-related processes are important for quiescence.

Author Manuscript Author Manuscript Author Manuscript Author Manuscript

LDs are nutrient reservoirs, and senescence can increase LD stores (Flor et al., 2017). However, a major knowledge gap is whether LDs are required for senescence or merely its byproduct. Here, we resolve this controversy in yeast by examining the LD marker Erg6 in post-AGR cell fate. As expected, AGR increased Erg6 signal and neutral lipids, consistent with elevated lipid storage. Surprisingly, LDs were not required for cell fates, as yeast lacking the TG lipases (*tgl3,4,5ΔΔΔ*) and yeast devoid of LDs (*Δ*LD) displayed similar proportions of quiescent cells and only slightly reduced senescent cell numbers. Given that LDs are storage organelles for long-term (i.e., multi-day) starvation, this may indicate that LDs are dispensable for relatively short-term (i.e., multi-hour) adaptations to nutrient shortage.

Since senescent cells failed to resume budding upon glucose replenishment, we interrogated whether they could respond to external cues and focused on their ability to traffic Mup1. Although the majority of the senescent cells endocytosed Mup1, half of those that endocytosed it did not deliver Mup1 into the vacuole degradation. This protein-sorting defect may be due to altered endomembrane trafficking and/or perturbed vacuole homeostasis, in line with the altered signatures of Vma1-mNeptune2.5 for senescence cells. An intact vacuole is necessary for cell-cycle progression (Jin and Weisman, 2015). Also, the vacuole-localized TORC1-Sch9 pathway can only signal from a mature functional vacuole, which may be compromised in senescence. Organelle homeostasis has been linked to cell fate responses in starvation, as mitochondrial morphology was found to be predictive of whether a cell will proliferate after starvation (Bagamery et al., 2020; Laporte et al., 2018). This indicates that organelle function is tightly connected to cell-cycle progression and fate determination.

We identified Rim15 as a biomarker providing early fate predictive capacity in our experimental system. Rim15 is a naturally low-abundant nutrient signaling kinase whose signal prior to AGR accurately predicted post-AGR cell fate. This supports a model where natural variation in the abundance of a nutrient-sensing effector is important to decision-making since cells must initiate fast responses to acute nutrient loss with existing protein machinery. It also indicates that long-term monitoring of single cells reveals cell-cell differences and, ultimately, that stochastic effects prior to starvation can affect long-term cellular responses.

In conclusion, we uncover noncanonical predictors of cell fate. Although these factors correlate with specific cell fates, their loss generally does not impact cell fate per se. For example, Nvj1, whose signal strongly correlates with quiescence, is not required for quiescence. Despite this, their predictive power highlights that in response to AGR, specific signaling pathways are tightly integrated with organelle homeostasis, metabolism, and, ultimately, cell decision-making.

Author Manuscript Author Manuscript Author Manuscript Author Manuscript

STAR★METHODS

RESOURCE AVAILABILITY

Lead Contact—Further information and requests for resources and reagents should be directed to and will be fulfilled by the Lead Contact, Mike Henne (mike.henne@utsouthwestern.edu).

Materials Availability—All unique/stable reagents generated in this study are available from the Lead Contact without restriction.

Data and Code Availability—The MATLAB software we used for segmentation and tracking can be downloaded with the supplementary of (Wood and Doncic, 2019). Other customized codes are available from the corresponding authors on request. The published article includes all datasets generated or analyzed during this study.

EXPERIMENTAL MODEL AND SUBJECT DETAILS

Media—The following media were used in this work: YPD (2% peptone, 1% yeast extract, 2% glucose), SC (1% succinic acid, 0.6% sodium hydroxide, 0.5% ammonium sulfate, 0.17% YNB (yeast nitrogen basewithout amino acids/ammonium sulfate), 0.113% dropout stock powder (complete amino acid)), SCD (SC with 2% glucose). SC and SCD-dropout media were made with dropout stock powder without methionine (SC-Met, SCD-Met). SC+Met and SCD+Met was made by adding methionine to SC-Met and SCD-Met to a final amount of 3.4 mg/ml methionine. Since we used pH sensitive fluorophore pHluorin, we checked the pH of the media and confirmed that SC, SCD, SC-Met, SCD-Met, SC+Met, and SCD+Met all have pH of 5.7–5.8.

Plasmid Construction—If not otherwise stated, all fluorophores were amplified from a plasmid template obtained from Addgene. The fluorophores were inserted into Longtine (pFA6a) (Longtine et al., 1998) plasmid backbones at PacI/AscI sites by DNA ligation or by PCR cloning kit (In-Fusion HD EcoDry Cloning kit, Clontech). All generated plasmids were confirmed by DNA sequencing.

Strain Construction—All strains used in this study are congenic with *S. cerevisiae* W303(leu2-3,112 his3-11,15 ura3-1 trp1-1 can1-100 ade2) (see Key Resources Table for a complete list of all strains used). Yeast cells were transformed using a standard PEG/lithium acetate protocol (Longtine et al.,1998), and all transformants were confirmed by PCR and microscopy. Diploid strains were constructed by crossing appropriate haploid strains. The diploid cells after the cross were selected according to their auxotrophic markers (HIS3, TRP1, LEU2 and URA3) or antibiotic markers hphMX, kanMX and natMX. When a selection marker was used for two different fluorophores, the strain was selected by PCR. Haploids were generated by tetrad dissection, which was performed using microscope Axio Scope.A1 (Zeiss), with a yeast dissection needle kit (Cora Styles Lab Supplies).

Author Manuscript Author Manuscript Author Manuscript Author Manuscript

METHOD DETAILS

Time-Lapse Microscopy—We used the same experimental setup as in Argüello-Miranda et al. (2018) except for magnification. Briefly, cells are imaged using a Zeiss Observer Z1 microscope equipped with automated hardware focus, motorized stage, temperature control, a Zeiss EC Plan-Apochromat 63X 1.4 oil immersion objective, and an AxioCam HRm Rev 3 camera. Each pixel corresponds to 0.205 μm. Excitation and emission filters, and dichroic mirrors used for each fluorophore are listed in Argüello-Miranda et al. (2018). For Vph1-GFP we used mNeongreen channel. Exposure times: Phase contrast 20ms, Whi5-mKoκ 150 ms, Erg6-mTFP1 20 ms, Vma1-mNeptune2.5 75ms, Nvj1-mRuby3 75ms, Msn2-mNeonGreen 40ms, Rtg1-mNeonGreen 40ms, or Rim15-mNeonGreen 100ms, Mup1-mKoκ 50ms, Mup1-pHluorin 50ms, Vph1-GFP 75ms.

Acute Glucose Restriction (AGR) Assay—All experiments were performed with a Y04C Cellasic microfluidic device (http://www.emdmillipore.com/cellasic) using a 0.6 or 1 psi flow rate. Images are taken every 6 minutes for 16 hr. Cells were taken from −80 freezer and grown on a YPD plate at 30°C for 24h. Next, a loop of cells is serially diluted in SCD and shaken overnight at 30°C to a final OD of 0.15–0.2. After sonication, 50 μL of cells are mixed with 50 μL of SCD and loaded to the microfluidics chamber. In the chamber, cells are first grown for 2hrs in SCD. Next, they are exposed to AGR by switching to SC for 10 hr which is followed by glucose replenishment by 4 hr SCD (Video S1). For Mup1 responsiveness assay, we used SC-Met in the first two hours of the assay, SC-Met or SC+Met for acute glucose restriction phase, and SC+Met for the replenishment phase (Videos S4, S5, and S6). To ensure that senescent cells are not simply delaying their cell cycle resumption, we also ran a 20 hr control experiment with 2 hr SCD, 10 hr SC, and 8hrs SCD.

Annotation of Cell Fates—For our analysis we used the cells that were born before AGR, where we define cell birth as the first Whi5-mKoκ nuclear entry. Buds are not included in our analysis. Cell fates are annotated semi-manually by using Whi5-mKoκ nuclear translocations and bud-growth/emergence from the phase contrast imaging using an interactive custom MATLAB software. If Whi5 is not tagged in the strain (e.g., strain used in Mup1 responsiveness assay), only bud growth is used to detect quiescent-committed cells during AGR. In these cases, some quiescence-committers might have been missed.

Senescent cell fate is not due to fitness issues—Given that these distinct cell fates may be attributable to pre-existing factors within the cell population, we investigated whether senescent and quiescent populations displayed distinct histories prior to AGR exposure. Our rationale centered on interrogating whether cells exhibited any detectable fitness defects during the pre-AGR phase. First, we investigated whether cell age correlates with distinct cell fates, and found that both quiescent and senescent cells can be of any age, and therefore cell fate in our system is not age dependent (See Replicative Age Determination, Table S4). This result is consistent with Laporte et al. (2018).

We also tested whether any cell population contained slow growing cells prior to AGR, which may indicate pre-existing fitness issues with them. We found no statistical difference

Author Manuscript Author Manuscript Author Manuscript Author Manuscript

in the doubling time of colonies compromised of only quiescent cells or senescent cells that preceded AGR (See Doubling Time Calculation, Table S5). We also monitored whether senescent cells were simply dead as a result of AGR stress. We first examined cell autofluoresce in multiple channels. Indeed, dead control cells displayed autofluorescence in multiple channels, but this was not observed in senescent cells. Furthermore, senescent cells maintained regular morphology in glucose replenished conditions, and displayed intact cellular structures by phase-contrast imaging (see dead versus senescent cells in Figure S1E). In addition, as discussed in the manuscript, senescent cells upregulate specific biomarkers during the AGR phase and respond to environmental cues during AGR that involve nuclear import of transcription factors, indicating these cells are not dead.

Finally, we investigated whether senescent cells were delaying cell cycle resumption upon glucose replenishment past the 4hrs post-AGR that we were monitoring. Extending our experimental protocol to 20hrs, we noted that 145 of 155 senescent cells failed to resume budding even 8hrs after glucose replenishment, indicating that the senescent cells were generally not re-starting their cell cycle. In addition, we verified that the senescent phenotype was not limited to cell lines with fluorescently tagged biomarkers; blank non-fluorescent cells also exhibited quiescent and senescent fates (79.3% (88/111) quiescent; 20.7% (23/111) senescent).

Collectively, our data indicate that single cells exhibit distinct fates during and after AGR stress, and these distinct fates are not simply explained by cell cycle phase upon AGR exposure, replicative age, doubling time, cell death, or delay in cell cycle resumption.

Lipid extraction Bligh and Dyer—Yeast cells were grown in the desired conditions and pelleted. Neutral lipids were extracted from whole cells using chloroform/methanol method modified from the Bligh and Dyer method (1959). After measuring the wet cell weight, pellets were lysed in cold room using glass bead–beating for 10 min in the presence of chloroform. Methanol was added, and the suspension was vortexed vigorously. Then, 500 mM NaCl prepared in 0.5% acetic acid was added to get the final concentration of chloroform:methanol:water to 2:2:1.8. Samples were spun at 4,000 rpm for 15 min in the cold room, and the bottom chloroform layer was recovered. Lipids were dried with Argon gas and dissolved in a small volume, typically 0.5 μl chloroform per 1 mg cell weight, and stored at −80°C.

Thin layer chromatography (TLC)—One-dimensional TLC was used to separate the extracted lipids using hexane:diethyl ether:acetic acid (80:20:1) as a solvent to separate neutral lipids. TLC silica plates (Millipore) were spray-stained with 3% copper (II) acetate prepared in 8% phosphoric acid. Stained plates were incubated in the oven at 145°C for 1 h to overnight to develop the bands. Stained TLC plates were scanned and then processed for quantification using Fiji (ImageJ). TLC plates were quantified using standards of known concentration.

QUANTIFICATION AND STATISTICAL ANALYSIS

Checking for Autofluorescence, Bleed-Through, and Signal-to-Noise Ratio —Note that we have used the fluorescent protein combination of mKoκ, mTFP1,

Author Manuscript Author Manuscript Author Manuscript Author Manuscript

mNeptune2.5, mNeongreen and mRuby3 in a single strain before and verified that we achieve high signal to noise ratio with our experimental setup (Argüello-Miranda et al., 2018). We tagged the proteins Whi5-mKoκ, Erg6-mTFP1, and Vma1-mNeptune2 together before, however we combined them with different proteins in mNeongreen and mRuby3 channels in this work. Thus, we repeated the bleed-through and signal-to-noise ratio analysis for one of our strains.

To this end, we compared the signal from a congenic blank strain with no fluorescent protein (YL184), 5-color WT-MSN2 strain, and 1-color strains with only one protein tagged (Table S1) by running our AGR assay with all these strains. We first verified that the mean intensity from the 1-color strains were significantly higher than that of blank cells in their respective channels (Kolmogorov-Smirnov test, $p < 0.001$). Next, we quantified the bleed-through in the system by first subtracting the average mean intensity of blank cells from the average mean intensity of every strain. Next, we scaled the average mean intensities to that of the 5-color WT-MSN2 strain (Table S1). Additionally, we calculated the signal to noise ratio in every channel by dividing the average mean intensity of the fluorophore in its channel by the maximum average mean intensity of the other fluorophores (Table S1). These quantifications are done at a time point when the signal of the tagged protein in its channel is brightest to account for the times of highest possibility of bleed-through. Thus, for mNeptune2.5 channel the quantifications are done before AGR, for mNeongreen at half an hour after AGR, and for mTFP1, mRuby3, and for mKoκ channels at the end of AGR. The mean intensity in the mRuby3 channel is calculated the way Nvj1 mean intensity is calculated as explained below in the parameter extraction section.

We noted that there is a slight bleed-through from Nvj1-mRuby3 channel to Whi5-mKoκ channel when the Nvj1 signal forms a localized bright patch. We corrected for this by subtracting one fourth of the processed Nvj1 channel image from the Whi5-Koκ channel. Note that although WT-RTG1 (PK1701) strain has Pdr16-CyoFP, we are not using this channel for this study due to the very low signal-to-noise ratio in the channel when our protein is used.

Cell Segmentation and Tracking—Cells are segmented and tracked using our previously published algorithm (Doncic et al., 2013; Wood and Doncic, 2019). The MATLAB software we used for segmentation and tracking can be downloaded with the supplementary of Wood and Doncic (2019).

Image Processing and Parameter Extraction—After cells are segmented and tracked, we processed the images and extracted parameters using custom MATLAB software (available upon request). Briefly, to increase the signal-to-noise ratio, we first applied filtering to the images. Specifically, we applied frequency domain filtering (Gonzalez and Woods, 2002) using the image_frequency_filter.m function available at https://www.mathworks.com/matlabcentral/fileexchange/53250-filtering-of-an-image-in-frequency-domain, MATLAB Central File Exchange, developed by Samudra Jagadish, retrieved October 2018. We used cutoff frequencies of 0.6 (Whi5-mKoκ, Nvj1-mRuby3) and 0.7 (Msn2-, Rtg1-, Rim15-mNeonGreen). Except for Vma1-mNeptune2.5 and Erg6-mTFP1 channels, where we used contraharmonic mean filter of order 2 with 3×3

Author Manuscript Author Manuscript Author Manuscript Author Manuscript

structuring element (Gonzalez and Woods, 2002) (code available upon request). Next, we determined non-cell pixels and subtracted from the image the average intensity of the non-cell pixels to remove background noise. To address the bleed-through from Nvj1-mRuby3 channel into Whi5-mKoκ channel (see above), we subtracted from Whi5-mKoκ channel images 1/4th of Nvj1-mRuby3 channel images. We used these processed images to extract the parameters below.

Cell size—The number of pixels that constitute the segmented cell. We will call these pixels 'cell pixels' below.

Mean intensity—The sum of cell pixel intensities divided by the cell size.

Nuclear intensity—The nucleus is segmented by fitting a 2D Gaussian to the brightest nuclear pixel as previously described (Doncic et al., 2013) and used (Argüello-Miranda et al., 2018).

Vacuolar and perivacuolar intensity—First, using the Vma1-mNeptune2.5 channel the location of the vacuole is determined. To this end, first the cell pixels that are above the mean intensity are segmented by thresholding. Next, connected components less than 3 pixels are removed and holes are filled using the bwareaopen and imfill MATLAB functions respectively. The resulting pixels are segmented as vacuolar pixels. The mean intensity of these pixels in the other channel (e.g., Mup1-mKoκ) is reported as the vacuolar and perivacuolar intensity. Note that this method captures signal that comes from within the vacuole, and signal that comes from the vacuole periphery, thus, we name it vacuolar and perivacuolar.

Plasma membrane intensity—The mean intensity of the pixels that constitute the outmost layer of the segmented cell, which is determined by applying imerode MATLAB function to the cell segmentation.

Coefficient of Variation (CoV)—CoV of the cell pixel intensities.

Nvj1 area—Pixels with intensities 1.5 standard deviation or higher than the mean are segmented by thresholding. Next, connected components less than 3 pixels are removed and holes are filled using the bwareaopen and imfill MATLAB functions respectively. The largest connected component is labeled as Nvj1 patch. The number of pixels that constitute the Nvj1 patch gives Nvj1 area.

Nvj1 mean intensity—On average mothers are 1000–1500 pixels, whereas Nvj1 signal is up to about 120 pixels. Thus, calculating mean intensity on the Nvj1-mRuby3 channel dilutes the signal and does not detect Nvj1 expansion. Therefore, we use the mean intensity of the 'Nvj1 patch pixels' described above as Nvj1 mean intensity.

Smoothing of the parameters—For each cell, the timeseries data over 16 hr is smoothened using the fit MATLAB function to apply smoothing spline with smoothing parameter of 0.7.

Author Manuscript Author Manuscript Author Manuscript Author Manuscript

Heatmap Ordering—First, cells are grouped by their fate. Next, cells of each fate are ordered by their traces during AGR. To this end, we first created an agglomerative hierarchical cluster tree using linkage MATLAB function. Next, we extracted the permutation from this tree using the dendogram MATLAB function with the number of leaf nodes equal to number of cells.

Cell Fate Prediction Framework—We pose the fate prediction of a given cell as a binary hypothesis testing problem, where we choose between the two hypotheses:

$$H: The\ cell\ will\ be\ quiescent\ (Quiescence).$$

$$\overline{H}: The\ cell\ will\ be\ senescent\ (Senescence).$$

To choose between the two hypotheses, we used *statistical evidence*, where $e(H|D)$, the evidence for H given the data D, is defined as the $10log_{10}$ of the posterior odds for H given data D,

$$e(H\,|\,D):\ = 10log_{10}O(H\,|\,D) = 10log_{10}O(H) + 10log_{10}\frac{p(D\,|\,H)}{p(D\,|\,\overline{H})},$$

where $O(H|D)$ is the posterior odds, and $O(H)$ is the prior odds. Note that $10log_{10}O(H)$ is also denoted as $e(H)$. Furthermore, if D has several components, i.e., $D = D_1D_2D_3\ldots D_n$, and D_i; D_j are logically independent for all i; $j \leq n$, then:

$$e(H\,|\,D) = e(H) + 10log_{10}\sum_{i=1}^{n}\left(\frac{p(D_i\,|\,H)}{p(D_i\,|\,\overline{H})}\right). \quad (1)$$

The derivation of statistical evidence from Bayes' theorem is presented in Jaynes (2003) and in the supplementary of Argüello-Miranda et al. (2018). Note that we used this framework to accurately predict the cell fates of cells undergoing meiosis or not well before the commitment to meiosis (Argüello-Miranda et al., 2018). This method is also known as Naive Bayes Classifier (Friedman et al., 2001). A thorough discussion of why Naive Bayes outperforms more complicated methods is given in Hand and Yu (2001).

Implementation of Statistical Evidence on Quiescence/Senescence Decision Making—To calculate $e(H|D)$, we estimated the two terms in Equation (1). For the first term, we assumed that the prior probabilities for H and $\overline{H}$ are equal, i.e., $p(H) = p(\overline{H})$, and thus, $e(H) = 10log_{10}(p(H)/p(\overline{H})) = 0$. We did not use the number of quiescent and senescent cells to estimate the prior odds for two reasons: First, we wanted to quantify the contribution of the measured parameters to the cell fate probabilities without a bias. Second, using the relative proportions would have reduced the cell fate predictions to a trivial problem: since the proportion of quiescent cells are significantly higher than the senescent cells, the prior

Author Manuscript Author Manuscript Author Manuscript Author Manuscript

would bias every prediction to be for quiescence, and the percentage of correct predictions would equal to the percentage of quiescent cells.

For the second term, we estimated $p(D_i|H)$ and $p(D_i \mid \overline{H})$ for every parameter D_i and cell using our data. First, we removed the cell, whose fate we will predict, from our pool of data. Next, we used the remaining cells to construct the population distributions for quiescent, P_Q, and senescent, P_S, cells for every time point (Figure 6A). To this end, we used kernel density estimations implemented by fitdist MATLAB function with the option of kernel distribution. We estimated the elements of the second term in (1) by:

$$\frac{p(D_i \mid H)}{p(D_i \mid \overline{H})} \approx \frac{P_Q(D_i)}{P_S(D_i)}.$$

Next, we predicted a cell to be quiescent, if $e(H|D) > 0$, and predicted senescent otherwise.

Pseudo-Gradient Search for Parameters to be used in Cell Fate Prediction— We first calculated the percentage of correctly predicted cells for every single parameter. Next, we grouped the parameters with high predictive power and used the combination that gave the highest number of correct predictions at the end of AGR in Figure 6.

Calculating the Probability of Quiescence/Senescence—To calculate the cell fate probabilities, we used the cells whose fate is correctly predicted at the end of AGR phase. Since $p(H \mid D) + p(\overline{H} \mid D) = 1$, we calculated the quiescence fate probability $p(H/D)$ solving the following equation for it:

$$\frac{p(H \mid D)}{p(\overline{H} \mid D)} = \frac{p(H \mid D)}{1 - p(H \mid D)} = \frac{p(H)}{p(\overline{H})} \frac{p(D \mid H)}{p(D \mid \overline{H})}$$

$$\approx 1 \prod_{i=1}^{n} \frac{P_Q(D_i)}{P_S(D_i)}.$$

Decision Point—Examining the evolution of cell fate probabilities throughout the AGR phase, we observed that cells have at first cell fate probabilities around 0.5. However, after a certain time point, the cell fate probabilities settle on one of the fates. We observed the same phenomenon in isogenic cell populations undergoing meiosis or not, and defined this time point as the *decision point* in Argüello-Miranda et al. (2018). In this work we extend this concept beyond meiosis.

The decision points are calculated by using the cells, whose fates are correctly predicted at the end of AGR. The decision point is defined as the time point, at and after which the cell fate predictions are always correct, i.e., the cell fate probability for the correct fate is above 0.5, until the end of the AGR phase.

Doubling Time Calculation—To compare the doubling times of quiescent cells and senescent before AGR, we calculated the doubling time of the cell colonies in the 2 hr of

Author Manuscript Author Manuscript Author Manuscript Author Manuscript

rich medium before AGR (Table S5). To estimate the quiescent cell doubling time, we used colonies made up of completely quiescent cells. For senescent cells this was not possible, because there were few colonies made up of all senescent cells. Thus, to estimate the senescent cell doubling time we used colonies made up of either only senescent cells or a mixture of quiescent and senescent cells, where senescent cells also undergo cell division (i.e., we did not include colonies that have senescent cells with replicative age 0). We counted the number of cells during the first 2 hr (i.e., 20 frames imaged every 6 min) of our assay using a custom interactive MATALB code (available upon request). Since during this phase cell are growing exponentially, we estimated the doubling time by fitting the number of cells to the function $y = ae^{kt}$, where y is the number of cells, t is time, and a and k are constants. The constant k is estimated utilizing the polyfit MATLAB function and the doubling time is given by $t_{Doubling} = (ln2 / k)$. Note that we removed outliers using the rmoutliers MATLAB function, which removes data points that are more than three scaled median absolute deviations. This ended up removing two outlier colony doubling times from WT-MSN2 senescent cells and two outliers from WT-RTG1 quiescent cells. With the outliers the doubling time for WT-MSN2 senescent cells is 103.4 ± 27.7 min with 120 final cells, and for WT-RTG1 quiescent cells it is 100.1 ± 22.6 with 142 final cells. This does not affect our conclusion that doubling times of quiescent and senescent colonies are not significantly different. Two-sample Kolmogorov-Smirnov test does not reject that the quiescent- and senescent-colony doubling times come from the same continuous distribution at 0.01 significance level (with outliers: p = 0.83 WT-MSN2, p = 0.0355 WT-RTG1, p = 0.29 combined, without outliers: p = 0.98 WT-MSN2, p = 0.12 WT-RTG1, p = 0.55 combined).

Replicative Age Determination—The replicative age of the cells born inside the microfluidics device is determined semi-manually using a custom-made interactive MATLAB code (Table S4). We define cell birth as the first nuclear entry of Whi5-mKoκ. Thus, cells that have a first Whi5-mKoκ nuclear entry, but has not budded themselves, are counted as of replicative age 0. Cells that budded once and twice are counted as of replicative age 1 and 2 respectively. Cells that were loaded to the microfluidics chamber at the beginning of the experiment are counted as cells of replicative age > 2. Note that we estimate these cells to have a replicative age less than 13, given that in our assay we take cells from a YPD plate, and then dilute to a very low OD of ~0.02 in SCD. Given that the doubling time of our strain is about 90 min in SCD at 30°C and that the cells grow under this condition for at most for about 20 hours, we expect the cells to make at most about 13 divisions. For w303-1a mean replicative lifespan is 24 ± 8 (mean ± SD) with a maximum of 39 (Zadrag-Tecza et al., 2009), thus, the cells in our assay are relatively young. The chi-square test does not reject the hypothesis that replicative age > 2 versus = < 2 is independent of the cell fate (p = 0.62 WT-MSN2, p = 0.89 WT-RTG1, p = 0.64 combined).

Quantification of Population Percentages with Detectable Signal—To quantify the senescent cells that have a detectable nuclear Whi5-mKoκ we first calculated a threshold for a detectable Whi5 signal. To this end, we calculated the average nuclear intensity of quiescent-committed cells over the last three time points of the AGR, since all of these cells had nuclear signal. Next, we calculated the mean and standard deviation of these, and

Author Manuscript Author Manuscript Author Manuscript Author Manuscript

accepted 2 standard deviations below the mean as a detectable nuclear signal. Next, we averaged the nuclear Whi5 signal over the last three time points of AGR and labeled cells that have this value higher than the basal value as having a detectable Whi5 signal.

To quantify the percentage of cells with extended Msn2 and Rtg1 signals, first, we calculated the basal nuclear intensities in these channels by averaging the nuclear intensity over the half hour before AGR. Next, we calculated the nuclear intensity between six and seventh hour of AGR and labeled cells that have more than 4 times the basal intensity for Msn2 and more than twice the basal intensity for Rtg1 as having extended signal.

To quantify the Nvj1 expansion, we first calculated the basal Nvj1 area (i.e., basal number the automated code detects when there is no Nvj1 expansion) by averaging the Nvj1 area over the last three frames before AGR. Next, we compared this basal value to the average Nvj1 area over the last hour of AGR. We labeled cells that have more than 1.2 times the basal area as having a Nvj1 expansion.

Chi-Square Test for Dependence of Cell Fate on Cell Cycle Stage—Quiescent-committed versus quiescent-arrested cell fate depends on the cell cycle stage (pre-/post-Start) the cell is in at the initiation of AGR ($p < 0.001$ WT-MSN2, $p < 0.001$ WT-RTG1, $p < 0.001$ combined, Chi-Square Test).

The chi-square test does not reject the hypothesis that quiescence/senescence cell fate is independent of the cell cycle stage of the cells at the time of AGR initiation at 0.01 significance level ($p = 0.24$ for WT-MSN2, $p = 0.05$ for WT-RTG1, $p = 0.02$ combined).

Supplementary Material

Refer to Web version on PubMed Central for supplementary material.

ACKNOWLEDGMENTS

We thank S. Schmid, J. Friedman, M. Lin, and J. Ewald for critical feedback. We also thank J. Goodman, Y. Liu, S. Rogers, N. Ortiz, O. Argüello-Miranda, and J. Noh for reagents and technical assistance. We also acknowledge friend and departed colleague Andreas Doncic, whose achievements served as a foundation for this work. N.E.W. is supported by grants from CPRIT (RR150058) obtained by Andreas Doncic and UTSW funds associated with Sandra Schmid. W.M.H. and H.H. are supported by funds from the Welch Foundation (I-1873), NIH NIGMS (GM119768), Ara Parseghian Fund (APMRF2020), and UTSW Endowed Scholars Program.

REFERENCES

Ai HW, Henderson JN, Remington SJ, and Campbell RE (2006). Directed evolution of a monomeric, bright and photostable version of Clavularia cyan fluorescent protein: structural characterization and applications in fluorescence imaging. Biochem. J 400, 531–540. [PubMed: 16859491]

Aragon AD, Rodriguez AL, Meirelles O, Roy S, Davidson GS, Tapia PH, Allen C, Joe R, Benn D, and Werner-Washburne M (2008). Characterization of differentiated quiescent and nonquiescent cells in yeast stationary-phase cultures. Mol. Biol. Cell 19, 1271–1280. [PubMed: 18199684]

Argüello-Miranda O, Liu Y, Wood NE, Kositangool P, and Doncic A (2018). Integration of Multiple Metabolic Signals Determines Cell Fate Prior to Commitment. Mol. Cell 71, 733–744.e11. [PubMed: 30174289]

Bagamery LE, Justman QA, Garner EC, and Murray AW (2020). A Putative Bet-hedging strategy buffers budding yeast against environmental instability. Curr. Biol 10.1016/j.cub.2020.08.092.

Author Manuscript Author Manuscript Author Manuscript Author Manuscript

Balázsi G, van Oudenaarden A, and Collins JJ (2011). Cellular decision making and biological noise: from microbes to mammals. Cell 144, 910–925. [PubMed: 21414483]

Broach JR (2012). Nutritional control of growth and development in yeast. Genetics 192, 73–105. [PubMed: 22964838]

Butow RA, and Avadhani NG (2004). Mitochondrial signaling: the retrograde response. Mol. Cell 14, 1–15. [PubMed: 15068799]

Chen J, Sutter BM, Shi L, and Tu BP (2017). GATOR1 regulates nitrogenic cataplerotic reactions of the mitochondrial TCA cycle. Nat. Chem. Biol 13, 1179–1186. [PubMed: 28920930]

Chu J, Haynes RD, Corbel SY, Li P, González-Gonzaález E, Burg JS, Ataie NJ, Lam AJ, Cranfill PJ, Baird MA, et al. (2014). Non-invasive intravital imaging of cellular differentiation with a bright red-excitable fluorescent protein. Nat. Methods 11, 572–578. [PubMed: 24633408]

Cross FR (1995). Starting the cell cycle: what's the point? Curr. Opin. Cell Biol 7, 790–797. [PubMed: 8608009]

Day A, Markwardt J, Delaguila R, Zhang J, Purnapatre K, Honigberg SM, and Schneider BL (2004). Cell size and Cln-Cdc28 complexes mediate entry into meiosis by modulating cell growth. Cell Cycle 3, 1433–1439. [PubMed: 15611626]

De Virgilio C (2012). The essence of yeast quiescence. FEMS Microbiol. Rev 36, 306–339. [PubMed: 21658086]

Dechant R, Binda M, Lee SS, Pelet S, Winderickx J, and Peter M (2010). Cytosolic pH is a second messenger for glucose and regulates the PKA pathway through V-ATPase. EMBO J 29, 2515–2526. [PubMed: 20581803]

Di Talia S, Skotheim JM, Bean JM, Siggia ED, and Cross FR (2007). The effects of molecular noise and size control on variability in the budding yeast cell cycle. Nature 448, 947–951. [PubMed: 17713537]

Doncic A, Falleur-Fettig M, and Skotheim JM (2011). Distinct interactions select and maintain a specific cell fate. Mol. Cell 43, 528–539. [PubMed: 21855793]

Doncic A, Eser U, Atay O, and Skotheim JM (2013). An algorithm to automate yeast segmentation and tracking. PLoS ONE 8, e57970. [PubMed: 23520484]

Flor AC, Wolfgeher D, Wu D, and Kron SJ (2017). A signature of enhanced lipid metabolism, lipid peroxidation and aldehyde stress in therapy-induced senescence. Cell Death Discov 3, 17075. [PubMed: 29090099]

Friedlander G, Joseph-Strauss D, Carmi M, Zenvirth D, Simchen G, and Barkai N (2006). Modulation of the transcription regulatory program in yeast cells committed to sporulation. Genome Biol 7, R20. [PubMed: 16542486]

Friedman J, Hastie T, and Tibshirani R (2001). The elements of statistical learning (Springer).

Gonzalez RC, and Woods ER (2002). Digital Image Processing (Addison-Wesley).

Görner W, Durchschlag E, Wolf J, Brown EL, Ammerer G, Ruis H, and Schüller C (2002). Acute glucose starvation activates the nuclear localization signal of a stress-specific yeast transcription factor. EMBO J 21, 135–144. [PubMed: 11782433]

Graham LA, Flannery AR, and Stevens TH (2003). Structure and assembly of the yeast V-ATPase. J. Bioenerg. Biomembr 35, 301–312. [PubMed: 14635776]

Hand DJ, and Yu K (2001). Idiot's Bayes—not so stupid after all? Int. Stat. Rev 69, 385–398.

Hariri H, Rogers S, Ugrankar R, Liu YL, Feathers JR, and Henne WM (2018). Lipid droplet biogenesis is spatially coordinated at ER-vacuole contacts under nutritional stress. EMBO Rep 19, 57–72. [PubMed: 29146766]

Henne WM, and Hariri H (2018). Endoplasmic Reticulum-Vacuole Contact Sites ''Bloom'' With Stress-Induced Lipid Droplets. Contact (Thousand Oaks) 1, 2515256418756112.

Henne WM, Buchkovich NJ, Zhao Y, and Emr SD (2012). The endosomal sorting complex ESCRT-II mediates the assembly and architecture of ESCRT-III helices. Cell 151, 356–371. [PubMed: 23063125]

Henne WM, Zhu L, Balogi Z, Stefan C, Pleiss JA, and Emr SD (2015). Mdm1/Snx13 is a novel ER-endolysosomal interorganelle tethering protein. J. Cell Biol 210, 541–551. [PubMed: 26283797]

Author Manuscript Author Manuscript Author Manuscript Author Manuscript

Honigberg SM (2016). Similar environments but diverse fates: Responses of budding yeast to nutrient deprivation. Microb. Cell 3, 302–328. [PubMed: 27917388]

Jacquier N, Choudhary V, Mari M, Toulmay A, Reggiori F, and Schneiter R (2011). Lipid droplets are functionally connected to the endoplasmic reticulum in Saccharomyces cerevisiae. J. Cell Sci 124, 2424–2437. [PubMed: 21693588]

Jaynes ET (2003). Probability theory: The logic of science (Cambridge University Press).

Jin Y, and Weisman LS (2015). The vacuole/lysosome is required for cell-cycle progression. eLife 4, e08160. [PubMed: 26322385]

Jorgensen P, Nishikawa JL, Breitkreutz B-J, and Tyers M (2002). Systematic identification of pathways that couple cell growth and division in yeast. Science 297, 395–400. [PubMed: 12089449]

Joyner RP, Tang JH, Helenius J, Dultz E, Brune C, Holt LJ, Huet S, Müller DJ, and Weis K (2016). A glucose-starvation response regulates the diffusion of macromolecules. eLife 5, e09376. [PubMed: 27003290]

Kohlwein SD, Veenhuis M, and van der Klei IJ (2013). Lipid droplets and peroxisomes: key players in cellular lipid homeostasis or a matter of fat–store ‘em up or burn ‘em down. Genetics 193, 1–50. [PubMed: 23275493]

Kristan K, and Rižner TL (2012). Steroid-transforming enzymes in fungi. J. Steroid Biochem. Mol. Biol 129, 79–91. [PubMed: 21946531]

Kvam E, and Goldfarb D (2006). Nucleus–vacuole junctions in yeast: anatomy of a membrane contact site (Portland Press Ltd.).

Lang MJ, Martinez-Marquez JY, Prosser DC, Ganser LR, Buelto D, Wendland B, and Duncan MC (2014). Glucose starvation inhibits autophagy via vacuolar hydrolysis and induces plasma membrane internalization by down-regulating recycling. J. Biol. Chem 289, 16736–16747. [PubMed: 24753258]

Laporte D, Gouleme L, Jimenez L, Khemiri I, and Sagot I (2018). Mitochondria reorganization upon proliferation arrest predicts individual yeast cell fate. eLife 7, e35685. [PubMed: 30299253]

Lawless C, Holman SW, Brownridge P, Lanthaler K, Harman VM, Watkins R, Hammond DE, Miller RL, Sims PF, Grant CM, et al. (2016). Direct and absolute quantification of over 1800 yeast proteins via selected reaction monitoring. Mol. Cell. Proteomics 15, 1309–1322. [PubMed: 26750110]

Liao X, and Butow RA (1993). RTG1 and RTG2: two yeast genes required for a novel path of communication from mitochondria to the nucleus. Cell 72, 61–71. [PubMed: 8422683]

Lin CH, MacGurn JA, Chu T, Stefan CJ, and Emr SD (2008). Arrestin-related ubiquitin-ligase adaptors regulate endocytosis and protein turnover at the cell surface. Cell 135, 714–725. [PubMed: 18976803]

Lizardo DY, Lin Y-L, Gokcumen O, and Atilla-Gokcumen GE (2017). Regulation of lipids is central to replicative senescence. Mol. Biosyst 13, 498–509. [PubMed: 28128379]

Longtine MS, McKenzie A 3rd, Demarini DJ, Shah NG, Wach A, Brachat A, Philippsen P, and Pringle JR (1998). Additional modules for versatile and economical PCR-based gene deletion and modification in Saccharomyces cerevisiae. Yeast 14, 953–961. [PubMed: 9717241]

Martínez-Pastor MT, Marchler G, Schüller C, Marchler-Bauer A, Ruis H, and Estruch F (1996). The Saccharomyces cerevisiae zinc finger proteins Msn2p and Msn4p are required for transcriptional induction through the stress response element (STRE). EMBO J 15, 2227–2235. [PubMed: 8641288]

Murley A, Sarsam RD, Toulmay A, Yamada J, Prinz WA, and Nunnari J (2015). Ltc1 is an ER-localized sterol transporter and a component of ER-mitochondria and ER-vacuole contacts. J. Cell Biol 209, 539–548. [PubMed: 25987606]

Newman JR, Ghaemmaghami S, Ihmels J, Breslow DK, Noble M, De-Risi JL, and Weissman JS (2006). Single-cell proteomic analysis of S. cerevisiae reveals the architecture of biological noise. Nature 441, 840–846. [PubMed: 16699522]

Pan X, Roberts P, Chen Y, Kvam E, Shulga N, Huang K, Lemmon S, and Goldfarb DS (2000). Nucleus-vacuole junctions in Saccharomyces cerevisiae are formed through the direct interaction of Vac8p with Nvj1p. Mol. Biol. Cell 11, 2445–2457. [PubMed: 10888680]

Author Manuscript Author Manuscript Author Manuscript Author Manuscript

Qu Y, Jiang J, Liu X, Wei P, Yang X, and Tang C (2019). Cell cycle inhibitor Whi5 records environmental information to coordinate growth and division in yeast. Cell Rep 29, 987–994.e985. [PubMed: 31644918]

Radulovic M, Knittelfelder O, Cristobal-Sarramian A, Kolb D, Wolinski H, and Kohlwein SD (2013). The emergence of lipid droplets in yeast: current status and experimental approaches. Curr. Genet 59, 231–242. [PubMed: 24057105]

Roberts P, Moshitch-Moshkovitz S, Kvam E, O'Toole E, Winey M, and Goldfarb DS (2003). Piecemeal microautophagy of nucleus in Saccharomyces cerevisiae. Mol. Biol. Cell 14, 129–141. [PubMed: 12529432]

Sagot I, and Laporte D (2019). The cell biology of quiescent yeast - a diversity of individual scenarios. J. Cell Sci 132, jcs213025.

Schmitt AP, and McEntee K (1996). Msn2p, a zinc finger DNA-binding protein, is the transcriptional activator of the multistress response in Saccharomyces cerevisiae. Proc. Natl. Acad. Sci. USA 93, 5777–5782. [PubMed: 8650168]

Seo AY, Lau P-W, Feliciano D, Sengupta P, Gros MAL, Cinquin B, Larabell CA, and Lippincott-Schwartz J (2017). AMPK and vacuole-associated Atg14p orchestrate m-lipophagy for energy production and long-term survival under glucose starvation. eLife 6, e21690. [PubMed: 28394250]

Smets B, Ghillebert R, De Snijder P, Binda M, Swinnen E, De Virgilio C, and Winderickx J (2010). Life in the midst of scarcity: adaptations to nutrient availability in Saccharomyces cerevisiae. Curr. Genet 56, 1–32. [PubMed: 20054690]

Wang C-W (2015). Lipid droplet dynamics in budding yeast. Cell. Mol. Life Sci 72, 2677–2695. [PubMed: 25894691]

Werner-Washburne M, Roy S, and Davidson GS (2011). Aging and the survival of quiescent and non-quiescent cells in yeast stationary-phase cultures. In Aging research in yeast (Springer), pp. 123–143.

Wood NE, and Doncic A (2019). A fully-automated, robust, and versatile algorithm for long-term budding yeast segmentation and tracking. PLoS ONE 14, e0206395. [PubMed: 30917124]

Zadrag-Tecza R, Kwolek-Mirek M, Bartosz G, and Bilinski T (2009). Cell volume as a factor limiting the replicative lifespan of the yeast Saccharomyces cerevisiae. Biogerontology 10, 481–488. [PubMed: 18985429]

Author Manuscript Author Manuscript Author Manuscript Author Manuscript

Highlights

- Isogenic cells respond differentially to acute glucose removal
- There is metabolic control on cell-cycle progression at every cell-cycle stage
- Nucleus-vacuole junction (NVJ) expansion is a strong predictor of cell fate
- Rim15 abundance prior to nutrient stress predicts behavior after nutrient stress

Author Manuscript Author Manuscript Author Manuscript Author Manuscript

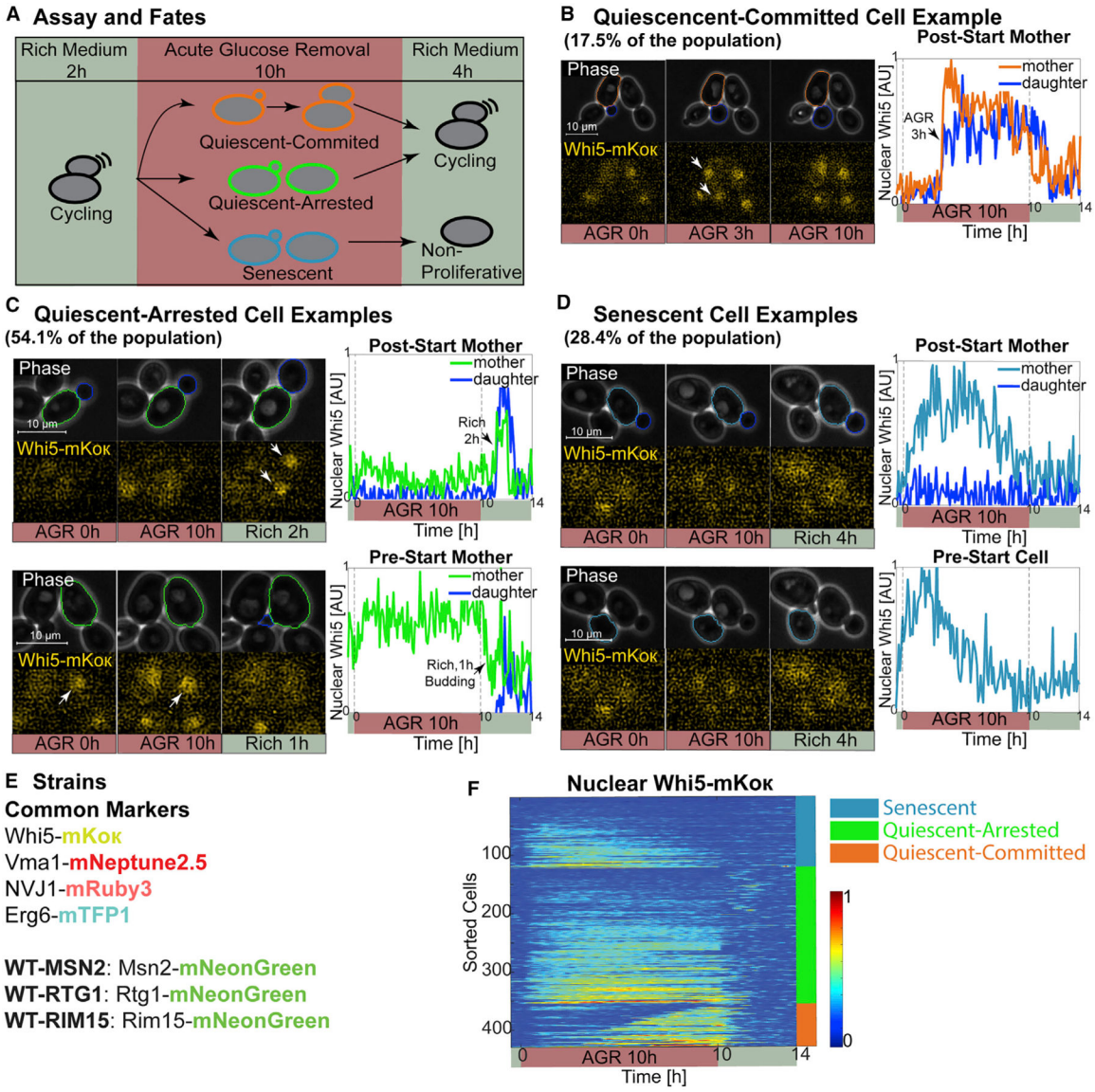

Figure 1. Isogenic Cells Respond Differentially to AGR

(A) Overview of assay. Cells are cycling before AGR. In AGR, quiescent-committed cells complete one cell cycle (orange). Quiescent-arrested (green) and senescent (blue) cells halt cell-cycle progression regardless of cell-cycle stage. Upon glucose replenishment, quiescent cells resume mitotic cycling; senescent cells do not.

(B) Example quiescent-committed cell. Mother cell has a small bud at AGR start (mother, orange; daughter, blue; AGR 0 h). During AGR, the bud grows, and the cell cycle is completed as seen by nuclear Whi5-mKoκ.

(C) Example quiescent-arrested cells. Top, post-Start mother (green) arrested with bud. Bottom, pre-Start cell (green).

(D) Example senescent cells. Senescent cells do not resume mitotic cycling, as seen from phase images and the lack of Whi5-mKoκ cycling.

(E) Strain list with fluorescent tags.

Author Manuscript Author Manuscript Author Manuscript Author Manuscript

(F) Nuclear Whi5-mKoκ traces for WT-MSN2 and WT-RTG1 strains. Cells are ordered by their cell fate, then ordered according to Whi5-mKoκ traces during AGR (n = 429).
See also Figure S1; Tables S1–S5; and Videos S1, S2, and S3.

Author Manuscript Author Manuscript Author Manuscript Author Manuscript

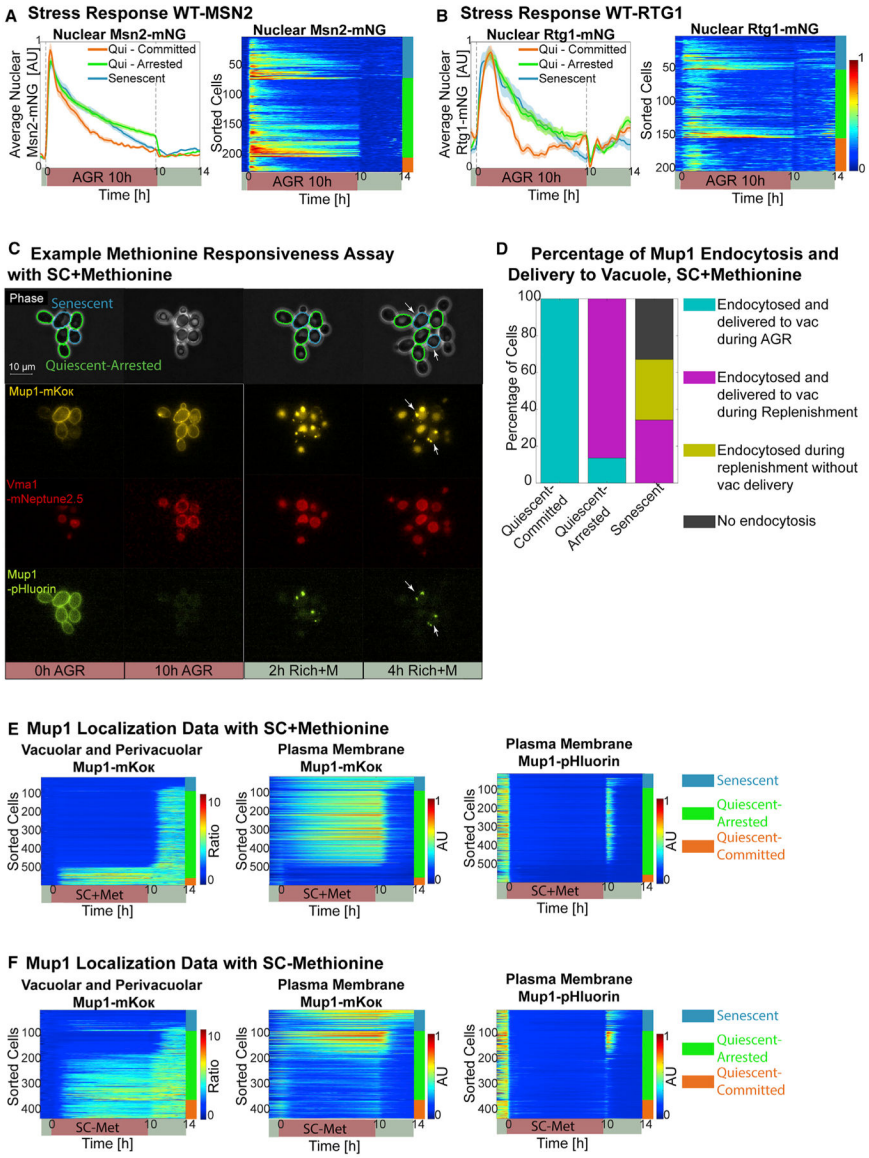

Figure 2. Senescent Cells Respond to Nutrient Stress and Environmental Cues

(A and B) Average nuclear Msn2-/Rtg1-mNeonGreen traces (mean ± SEM) and heatmap exhibiting individual cell traces using WT-MSN2 (n = 227) and WT-RTG1 (n = 202) strains, respectively.

(C) Example methionine (Met) responsiveness assay. AM44 cells grown in media lacking Met (SCD-Met) are exposed to AGR with SC media containing Met (SC+Met). Shown are senescent cells (blue) and quiescent-arrested cells (green). Note senescent cells uptake Mup1-mKoκ and Mup1-pHluorin, but do not sort into acidic vacuole. Vma1-mNeptune2.5 = vacuole. This colony also shown in Video S4.

(D) Percentage of cells that sort Mup1 by cell fate during Met assay with SC+Met (n = 585). vac, vacuole.

(E and F) Mup1 localization for Met assay with SC+/—Met using AM44 cells (n = 585/n = 428).

Author Manuscript Author Manuscript Author Manuscript Author Manuscript

See Figure S2; Table S2; and Videos S4, S5, and S6.

Author Manuscript Author Manuscript Author Manuscript Author Manuscript

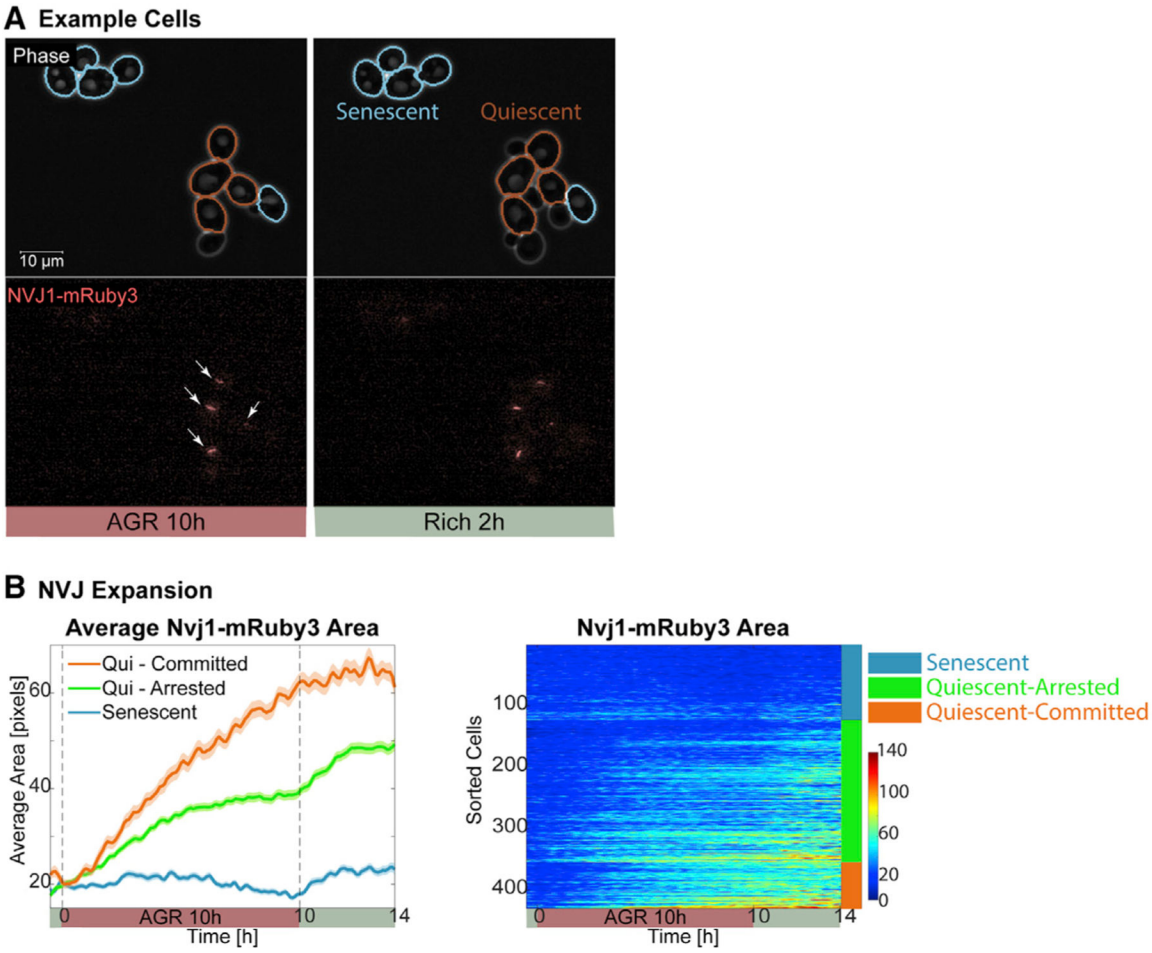

Figure 3. Quiescent Cells Enlarge Their NVJ in AGR, but Senescent Cells Do Not

(A) Example quiescent (brown) and senescent (blue) cells. Nvj1-mRuby3 expands in quiescent cells (white arrows); however, it does not in senescent cells. Colony also shown in Videos S1 and S3.

(B and C) NVJ expansion quantification for WT-MSN2 and WT-RTG1 (n = 429). Left: average Nvj1-mRuby3 area for quiescent-committed (orange), quiescent-arrested (green), and senescent (blue) (mean ± SEM). Right: cell traces as heatmap. Before AGR, cells do not expand Nvj1-mRuby3; software picks a roi for Nvj1-signal ~20 pixels.

See Figure S3; Table S2; and Videos S1, S2, and S3.

Author Manuscript Author Manuscript Author Manuscript Author Manuscript

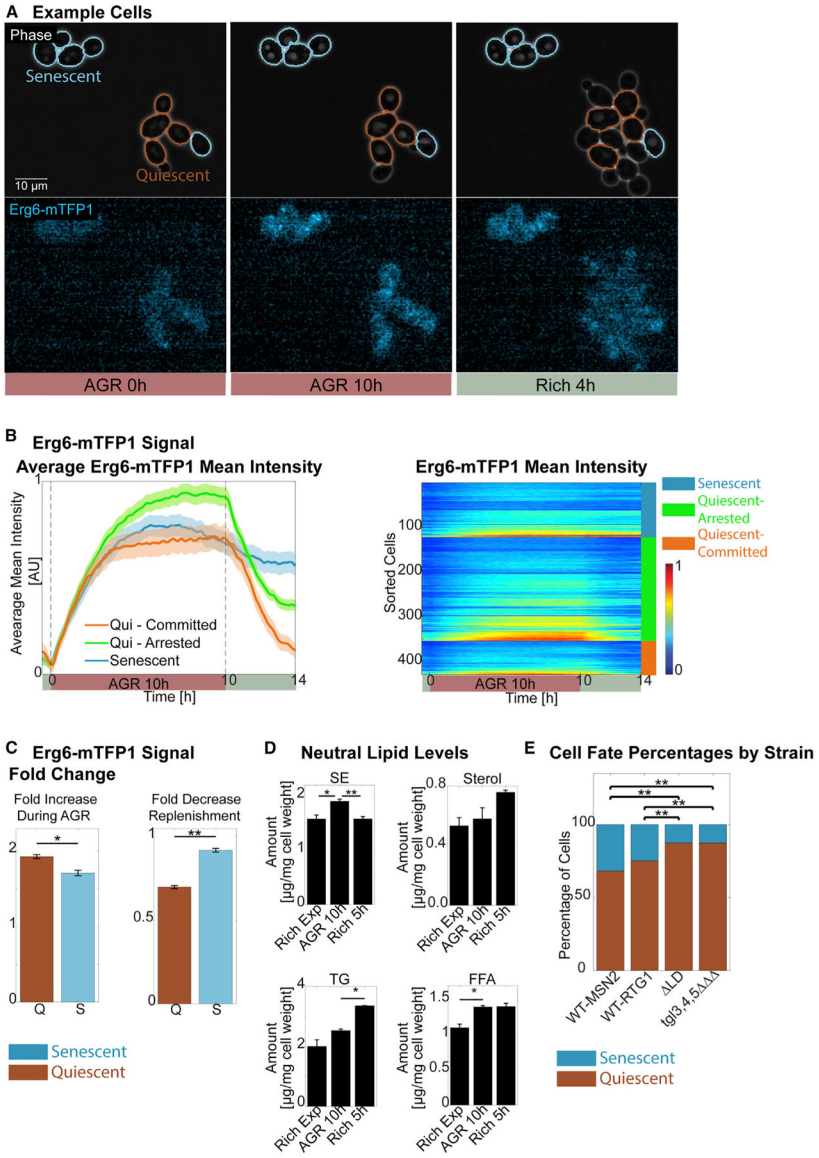

Figure 4. Cells Exhibit Enhanced Lipid Storage during AGR

(A) Example quiescent (brown) and senescent (blue) cells. Colony also shown in Videos S1 and S3.

(B) Erg6-mTFP1 signal for WT-MSN2 and WT-RTG1 cells (n = 429). Left: average Erg6-mTFP1 mean intensity (mean ± SEM). Right: cell traces for Erg6-mTFP1 mean intensity.

(C) Fold increase during AGR from determining ratio of the Erg6-mTFP1 mean intensity at AGR end and beginning (1.93 ± 0.03/1.71 ± 0.04 quiescent/senescent [n = 307/122 quiescent/senescent; mean ± SEM]). Fold decrease during replenishment calculated by ratio of Erg6-mTFP1 mean intensity at AGR end of 4-h replenishment to the end of AGR (0.70 ± 0.01/0.92 ± 0.01 quiescent/senescent [n = 307/122 quiescent/senescent; mean ± SEM]). Q, quiescent; S, senescent. *p < 0.05, **p < 0.01, Kolmogorov-Smirnov test.

(D) Neutral lipids from TLC. SE, sterol ester; TG, triglyceride; FFA, free fatty acid. *p < 0.05, **p < 0.01, t test. Experiment with YL184, two independent samples.

Author Manuscript Author Manuscript Author Manuscript Author Manuscript

(E) Cell fate percentage by strain (WT-MSN2 n = 227, WT-RTG1 n = 202, ΔLD n = 177, *tgl3,4,5*ΔΔΔ n = 239). **p < 0.01, Chi-square test.
See also Figure S4; Table S2; and Videos S1, S2, and S3.

Author Manuscript Author Manuscript Author Manuscript Author Manuscript

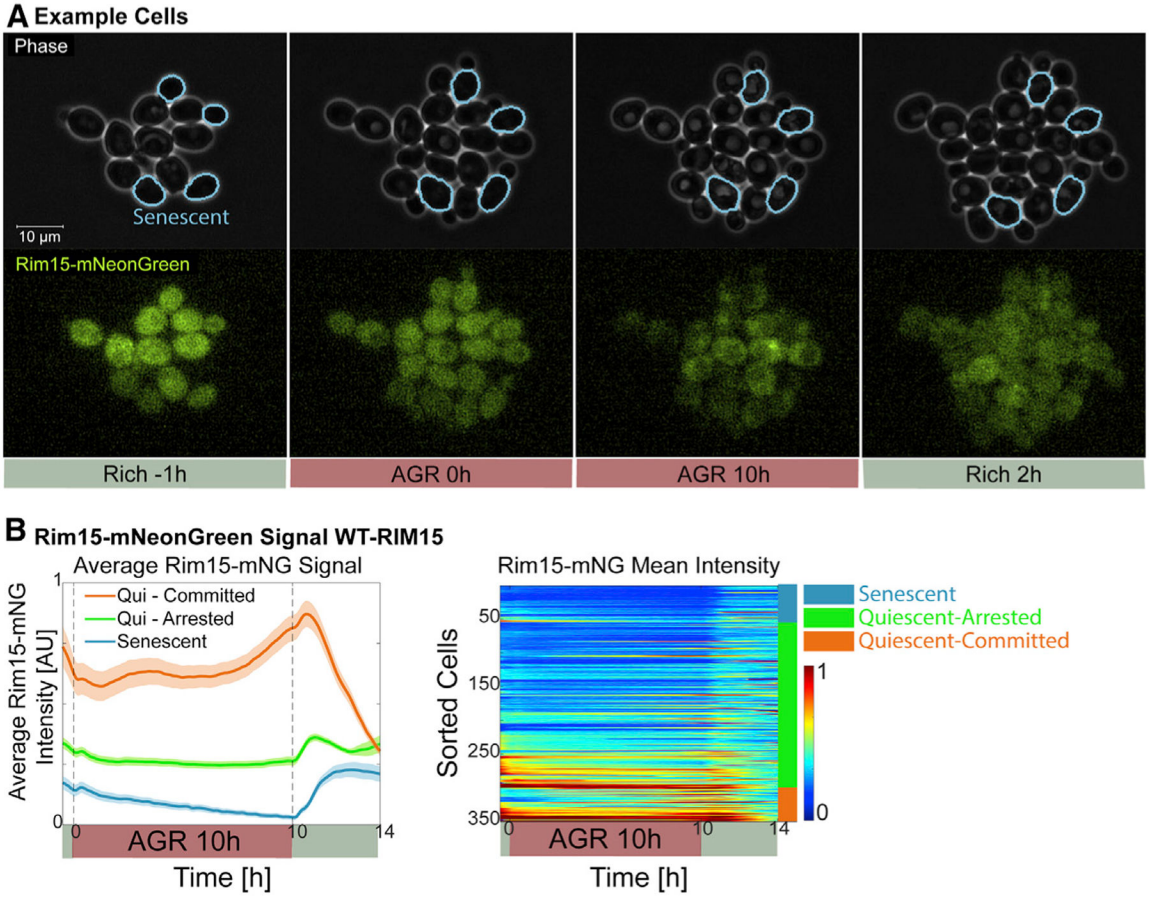

Figure 5. Pre-AGR Rim15 Levels Are Predictive of Post-AGR Cell Fate

(A) Example quiescent (unmarked) and senescent (blue) cells. Colony also shown in Video S7.

(B) Rim15-mNG signal using PK1811 and AM45 strains (n = 350). Left: average (mean ± SEM). Right: heatmap of cell traces.

See Figure S5, Table S2, and Video S7.

Author Manuscript Author Manuscript Author Manuscript Author Manuscript

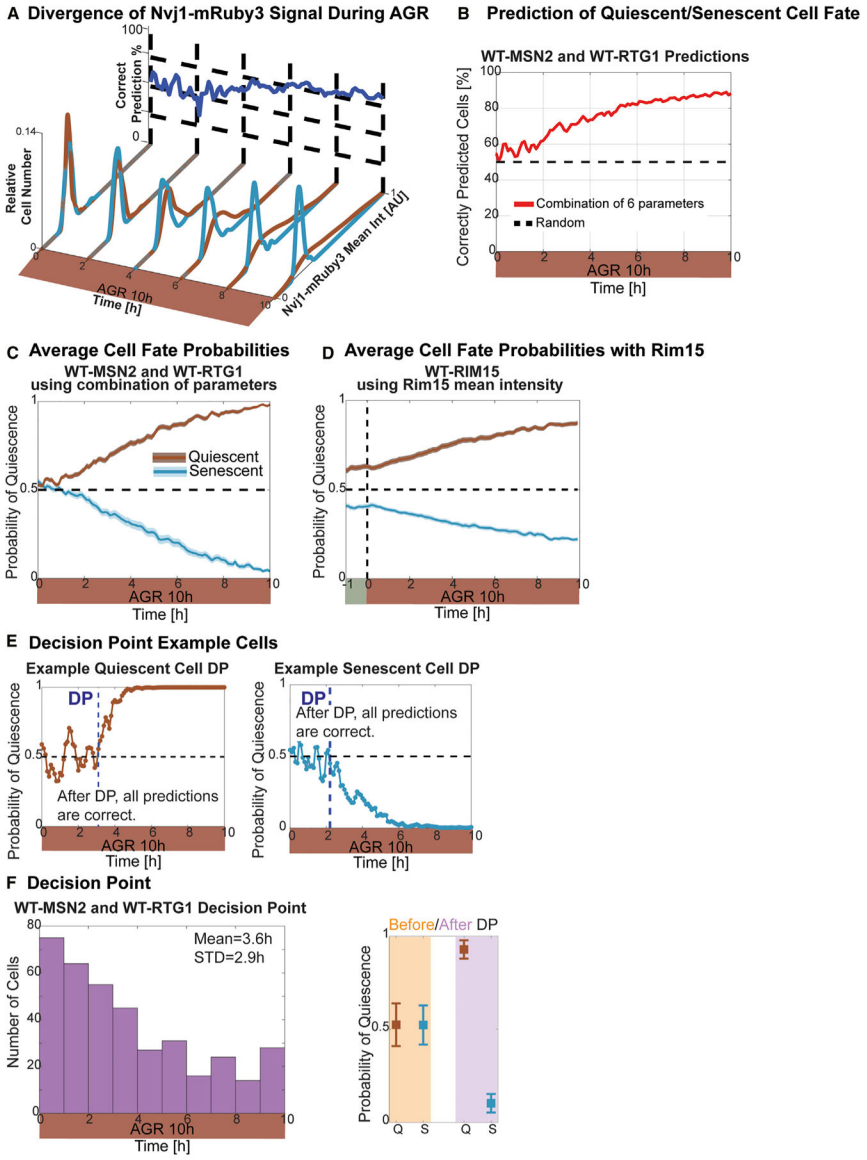

Figure 6. Cells ‘‘Decide’’ on Their Fate before Glucose Replenishment

(A) Quiescent (brown) and senescent (blue) Nvj1-mRuby3 mean intensity distributions in AGR and percentage of correctly predicted cells with these distributions (back axis, dark blue) using WT-MSN2 strain (n = 227).

(B) Percentage of correctly predicted cells, combination of multiple markers (red); WT-MSN2 and WT-RTG1 strains (n = 429). 50% marks random guess in binary decision (dashed line). See Figure S6A.

(C) Average quiescence fate probabilities for quiescent (brown) and senescent (blue) WT-MSN2 and WT-RTG1 strains calculated with marker combinations from (B), red line (n = 379). See Figures S6C and S6D.

(D) Average quiescence fate probabilities for quiescent (brown) and senescent (blue) cells calculated using Rim15-mNG mean intensity of PK1811 and AM45 strains (n = 253).

Author Manuscript Author Manuscript Author Manuscript Author Manuscript

(E) Evolution of quiescence fate probability for a quiescent (left, brown) and senescent (right, blue) cell; also shown is calculation of the DP.
(F) Left: the histogram of DP times. Right: average probability of quiescence before and after DP (mean ± SEM). WT-MSN2 and WT-RTG1 strains (n = 379). See Figure S6 and Table S2.

Author Manuscript Author Manuscript Author Manuscript Author Manuscript

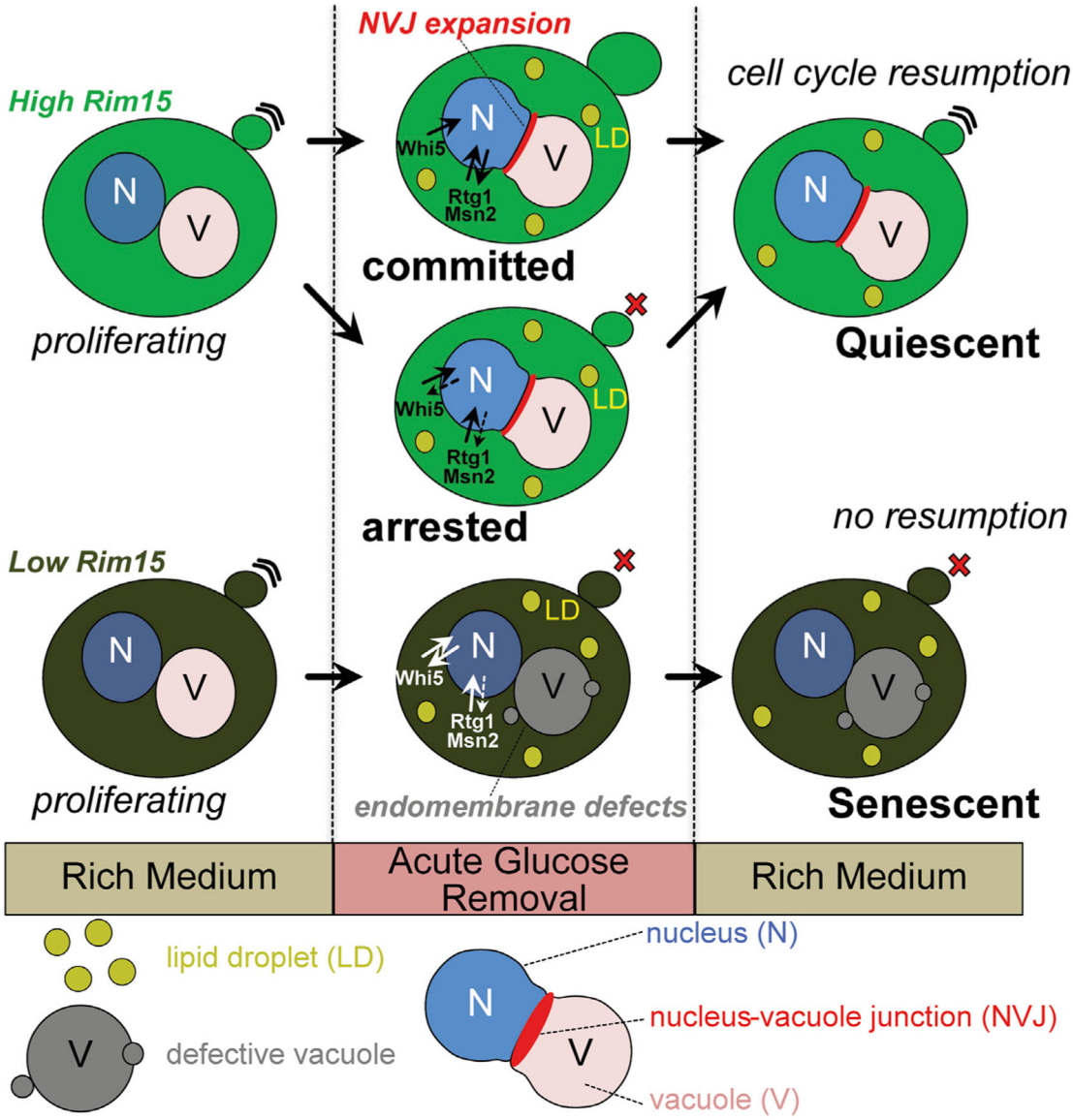

Figure 7. Working Model of Non-canonical Determinants in Cell Fate

Author Manuscript Author Manuscript Author Manuscript Author Manuscript

KEY RESOURCES TABLE

REAGENT or RESOURCE	SOURCE	IDENTIFIER
Chemical, peptides, and Recombinant Proteins		
G418 disulfate salt	Sigma-Aldrich	Cat# A1720
Nourseothricin sulfate (NAT)	Gold Biotechnology	Cat# N5001
Hygromycin B	Sigma-Aldrich	Cat# 10843555001
Yeast Nitrogen Base Without Amino Acids and Ammonium Sulfate	Sigma-Aldrich	Cat# Y1251
Zymolase	SUNRISE SCIENCE	Cat# N0766391
Phire hotstart II DNA Pollymerase	Thermo Fisher Scientific	Cat# F124L
Q5 High-Fidelity DNA Polymerase	NEW ENGLAND Biolabs	Cat# M0491L
Critical Commercial Assays		
In-Fusion HD EcoDry cloning Kit	Takara Bio USA	cat# 639690
ORGANISMS/STRAINS		
Saccharomyces cerevisiae W303 (leu2-3,112 trp1-1 can1-100 ura3-1 ade2-1 his3-11,15)	Saccharomyces GENOME DATABASE https://www.yeastgenome.org/strain/W303	N/A
YL184 *(MAT a/MATα, HIS3/his3, TRP1/trp1, LEU2/leu2, URA3/ura3, ADE2/ADE2)*	(Argüello-Miranda et al., 2018)	N/A
PK1273 *(MAT a/MATα, HIS3/his3, trp1/trp1, LEU2/leu2, URA3/ura3, ADE2/ADE2, WHI5/WHI5-mKOκ-TRP1)*	(Argüello-Miranda et al., 2018)	N/A
PK1359 *(MAT a/MATα, his3/his3, trp1/trp1, LEU2/leu2, URA3/ura3, ADE2/ADE2, ERG6/ERG6-mTFP-HIS3, WHI5/WHI5-mKOκ-TRP1, VMA1/VMA1-mNeptune2.5-kanMX6, NVJ1/NVJ1-mRuby3-hphMX6, MSN2/MSN2-mNeongreen(yeast optimized)-hphMX6)*	This Paper	N/A
PK1701 *(MAT a/MATα, his3/his3, trp1/trp1, LEU2/leu2, URA3/ura3, ADE2/ADE2, ERG6/ERG6-mTFP-HIS3, WHI5/WHI5-mKOκ-TRP1, VMA1/VMA1-mNeptune2.5-kanMX6, NVJ1/NVJ1-mRuby3-hphMX6, RTG1/RTG1-mNeongreen(yeast optimized)-natMX6, PDR16/PDR16-CyoFP1-hphMX6)*	This Paper	N/A
PK1261 *(MAT a/MATα, his3/his3, trp1/trp1, LEU2/leu2, URA3/ura3, ADE2/ADE2, ERG6/ERG6-mTFP-HIS3, WHI5/WHI5-mKOκ-TRP1, VMA1/VMA1-mNeptune2.5-kanMX6, nvj1::NAT/nvj1::NAT, MSN2/MSN2-mNeongreen(yeast optimized)-hphMX6, PDR16/PDR16-cyOFP-hphMX6)*	This Paper	N/A
PK1811 *(MAT a/MAT, his3/his3, trp1/trp1, LEU2/leu2, URA3/ura3, ADE2/ADE2, ERG6/ERG6-mTFP-HIS3, WHI5/WHI5-mKOκ-TRP1, VMA1/VMA1-mNeptune2.5-kanMX6, RIM15/RIM15-mNeongreen(yeast optimized)-natMX6, NVJ1/NVJ1-mRuby3-hphMX6)*	This Paper	N/A
AM45 (*MAT a/MATα, his3/his3, trp1/trp1, LEU2/leu2, ura3/ura3, ADE2/ADE2, ERG6/ERG6-mTFP-HIS3, WHI5/WHI5-mKOκ-TRP1, VMA1/VMA1-mNeptune2.5-kanMX6, RIM15/RIM15-mNeongreen(yeast optimized)-natMX6, NVJ1/NVJ1-mRuby3-hphMX6*)	This Paper	N/A
PK1786 *(MAT a/MATα, his3/his3, trp1/trp1, LEU2/leu2, URA3/ura3, ADE2/ADE2, ERG6/ERG6-mTFP-HIS3, tgl4::TRP1/tgl4::TRP1, VPH1/VPH1-GFP-kanMX6, tgl3::natMX6/tgl3::natMX6, tgl5::hphMX6/tgl5::hphMX6)*	This Paper	N/A
PK1790 *(MAT a/MATα, HIS3/his3, TRP1/trp1, LEU2/leu2, URA3/ura3, ADE2/ADE2, MUP1/MUP1-mKO-hphMX6)*	This Paper	N/A
PK1791 *(MAT a/MATα, HIS3/his3, TRP1/trp1, LEU2/leu2, URA3/ura3, ADE2/ADE2, MUP1/MUP1-pHluorin-natMX6)*	This Paper	N/A
PK1796 *(MAT a/MATα, HIS3/his3, TRP1/trp1, LEU2/leu2, URA3/ura3, ADE2/ADE2, VPH1/VPH1-GFP-kanMX6*)	This Paper	N/A
AM29 *(MAT a/MATα, his3/his3, trp1/trp1, leu2/leu2, ura3/ura3, ADE2/ADE2, are1::HIS3/are1::HIS3, lro1::LEU2/lro1::LEU2, are2::LEU2/are2::LEU2, dga1::URA3/dga1::URA3, ERG6/ERG6-mTFP-HIS3, WHI5/WHI5-mKOκ-TRP1, VMA1/VMA1-mNeptune2.5-kanMX6, NVJ1/NVJ1-mRuby3-hphMX6)*	This Paper	N/A
AM31 *(MAT a/f, HIS3/his3, TRP1/trp1, LEU2/leu2, URA3/ura3, ADE2/ADE2, PDR16/PDR16-cyOFP-hphMX6)*	This Paper	N/A

Author Manuscript Author Manuscript Author Manuscript Author Manuscript

REAGENT or RESOURCE	SOURCE	IDENTIFIER
AM32 *(MAT a/MATα, HIS3/his3, TRP1/trp1, LEU2/leu2, URA3/ura3, ADE2/ADE2, RTG1/RTG1-mNeongreen(yeast optimized)-hMX6)*	This Paper	N/A
AM33 *(MAT a/MATα, HIS3/his3, TRP1/trp1, LEU2/leu2, URA3/ura3, ADE2/ADE2, NVJ1/NVJ1-mRuby3-hphMX6)*	This Paper	N/A
AM34 *(MAT a/MATα, HIS3/his3, TRP1/trp1, LEU2/leu2, URA3/ura3, ADE2/ADE2, MSN2/MSN2-mNeongreen(yeast optimized)-hphMX6)*	This Paper	N/A
AM44 *(MAT a/MATα, HIS3/his3, TRP1/trp1, LEU2/leu2, URA3/ura3, ADE2/ADE2, VMA1/VMA1-mNeptune2.5-kanMX6, MUP1/MUP1-pHluorin-natMX6, MUP1/MUP1-mKOκ-hphMX6)*	This Paper	N/A
AM45 *(MAT a/MATα, his3/his3, trp1/trp1, LEU2/leu2, ura3/ura3, ADE2/ADE2, ERG6/ERG6-mTFP-HIS3, WHI5/WHI5-mKOκ-TRP1, VMA1/VMA1-mNeptune2.5-kanMX6, RIM15/RIM15-mNeongreen(yeast optimized)-natMX6, NVJ1/NVJ1-mRuby3-hphMX6)*	This Paper	N/A
OAM126 *(MAT a/MATα, his3/his3, TRP1/trp1, LEU2/leu2, URA3/ura3, ADE2/ADE2, ERG6/ERG6-mTFP-HIS3*)	(Argüello-Miranda et al., 2018)	N/A
OAM127 *(MAT a/MATα, HIS3/his3, TRP1/trp1, LEU2/leu2, URA3/ura3, ADE2/ADE2, VMA1/VMA1-mNeptune2.5-kanMX6)*	(Argüello-Miranda et al., 2018)	N/A
PK1708 *(MAT a/MATα, HI3/his3, TRP1/trp1, LEU2/leu2, URA3/ura3, ADE2/ADE2, RIM15/RIM15-mNeongreen(yeast optimized)-natMX6*)	This paper	N/A
Oligonucleotides		
Erg6-F: CGCCGAAACCCCCTCCCAAACTTCCCAAGAAGCA ACTCAACGGATCCCCGGGTTAATTAA	(Argüello-Miranda et al., 2018), C-terminal tagging following (Longtine et al., 1998).	N/A
Erg6-R: ATATCGTGCGCTTTATTTGAATCTTATTGATCTAG TGAATGAATTCGAGCTCGTTTAAAC;	(Argüello-Miranda et al., 2018), C-terminal tagging following (Longtine et al., 1998).	N/A
Vma1-F: TTGAGCACTATGCAAGAAAGATTTGCTGAATCT ACCGATCGGATCCCCGGGTTAATTAA;	(Argüello-Miranda et al., 2018), C-terminal tagging following (Longtine et al., 1998).	N/A
Vma1-R: CATCTAACAAATATACCAGAAGATAAATGCTACATA TATCGAATTCGAGCTCGTTTAAAC	(Argüello-Miranda et al., 2018), C-terminal tagging following (Longtine et al., 1998).	N/A
Rtg1-F: CTTCGAGTACGGAGGGTATGGTGAGTACGGTAATGG TAGCCGGATCCCCGGGTTAATTAA	This paper, C-terminal tagging following (Longtine et al., 1998).	N/A
Rtg1-R: GGTTATCACAACATAGCAATAGTGAGAGTCAGAAGT ACTTGAATTCGAGCTCGTTTAAAC	This paper, C-terminal tagging following (Longtine et al., 1998).	N/A
Nvj1-F: GATGCACAAGTGAACACTGAACAAGCATA CTCTCAACCATTTAGACGGATCCCCGGGTTAATTAA	C-terminal tagging following (Longtine et al., 1998).	N/A
Nvj1-R: CGTTGTAAGTGACGATGATAACCGAGATGACG GAAATATAGTACAGAATTCGAGCTCGTTTAAAC	C-terminal tagging following (Longtine et al., 1998).	N/A
Pdr16-F: GTACTCATGAAAAACTTCTTTACCCAGTAAAA TCGGAAAGCAGTACCGTGCGGATCCCCGGGTTAATTAA	C-terminal tagging following (Longtine et al., 1998).	N/A
Pdr16-R: CTCTTTTATTTATTATATATTATAGTGCATTATCATTATCTATCTAAATTTGCCTGAATTCGAGCTCGTTTAAAC	C-terminal tagging following (Longtine et al., 1998).	N/A
Mup1-F: GGCGTTATTGAAACGAATATAATCGAACATTACAAAAGTGAACAAGAAAAATCGCTGCGGATCCCCGG GTTAATTAA	C-terminal tagging following (Longtine et al., 1998).	N/A
Mup1-R: GAATGTTCATACGTGATTATAAGAATCGAGATGAGATGGTAAGTACCTTTTTGGGAATTCGAGCTCGTTTAAAC	C-terminal tagging following (Longtine et al., 1998).	N/A

Author Manuscript Author Manuscript Author Manuscript Author Manuscript

REAGENT or RESOURCE	SOURCE	IDENTIFIER
nvj1-KO-F: ATAATATCAAAAAAGCTACAAATATAATTGTA AAATATAATAAGCCGGATCCCCGGGTTAATTAA	C-terminal tagging following (Longtine et al., 1998).	N/A
nvj1-KO-R: CGTTGTAAGTGACGATGATAACCGAGATGACGGAAATATAGTACAGAATTCGAGCTCGTTTAAAC	C-terminal tagging following (Longtine et al., 1998).	N/A
Msn2-F: GTCGCAACACATCAAGACTCATAAAAAACATGGAGACATTCGGATCCCCGGGTTAATTAA	This paper, C-terminal tagging following (Longtine et al., 1998).	N/A
Msn2-R: TTATGAAGAAAGATCTATCGAATTCCCCCCCTGGGGTCTAGAATTCGAGCTCGTTTAAAC	This paper, C-terminal tagging following (Longtine et al., 1998).	N/A
Rim15-F: TGAAGAGCATACTATATTGAGCGATTCTGATGAAACGCACCGGATCCCCGGGTTAATTAA	This paper, C-terminal tagging following (Longtine et al., 1998).	N/A
Rim15-R: ATTCAGTTATTTTTTTTAATTATCTTTATCTTAAAATTTAGAATTCGAGCTCGTTTAAAC	This paper, C-terminal tagging following (Longtine et al., 1998).	N/A
Vph1-F: GGAAGTCGCTGTTGCTAGTGCAAGCTCTTCCGCTTCAAGCCGGATCCCCGGGTTAATTAA	This paper, C-terminal tagging following (Longtine et al., 1998).	N/A
Vph1-R: AGTACTTAAATGTTTCGCTTTTTTTAAAAGTCCTCAAAATGAATTXGAGCTCGTTTAAAC	This paper, C-terminal tagging following (Longtine et al., 1998).	N/A
RECOMBINANT DNA		
Plasmid, mTFP-N1	Addgene	Cat# 54521; (Ai, et al., 2006)
Plasmid, pYLB18 (mTFP-HIS3) backbone: pLongtine-mCitrine-HIS3, fluorophore sequence from: mTFP-N1	(Argüello-Miranda et al., 2018)	N/A
Plasmid, pcDNA3-mNeptune2.5	Addgene	Cat# 51310; (Chu et al., 2014)
Plasmid, pPKB3 (mNeptune2.5-kanMX6) backbone: pLongtine4, fluorophore sequence from: pcDNA3-mNeptune2.5	(Argüello-Miranda et al., 2018)	N/A
Plasmid, pYLB4 (mRuby3-hphMX6) backbone: pCA14, fluorophore sequence from: pc3.1-CAG-mRuby3-mTurquoise2 (Sandra Schmid lab)	This paper	N/A
Plasmid, pTSK437-YOmNG (yeast optimized mNeonGreen)	Allele Biotechnology	(Chu et al., 2014)
Plasmid, pYLB10 (mNeongreen (yeast optimized)-hphMx6) backbone: pCA14, Fluorophore sequence from: pTSK437-YOmNG mNeongreen (yeast optimized (Allele Biotechnology)	(Argüello-Miranda et al., 2018)	N/A
Plasmid, pYLB9 (mNeongreen (yeast optimized)-natMx6) backbone: pCA14, Fluorophore sequence from: pTSK437-YOmNG mNeongreen (yeast optimized (Allele Biotechnology)	This paper	N/A
Plasmid, pPKB8 (cyOFP-hphMx6) backbone: pCA17, fluorophore sequence from: Vector pLVXiPuro Tractin CyOFP (pW0085)(Fiolka lab)	This paper	N/A
Plasmid, pCA14 (mKOκ-hphMX6) backbone: pFA6a	Skotheim Lab, Stanford	(Longtine et al., 1998)
Plasmid Mup1-pHlourin::natMX6	Henne lab, derived from plasmid originally from C. Boone lab.	Henne, JCB, 2015
Software and Algorithms		
MATLAB	https://www.mathworks.com/products/MATLAB.html	RRID: SCR_001622

REAGENT or RESOURCE	SOURCE	IDENTIFIER
Cell segmentation and Tracking Algorithm	(Doncic et al., 2013; Wood and Doncic, 2019)	N/A

Author Manuscript
Author Manuscript
Author Manuscript
Author Manuscript